M2LW-16OR0402152
PNNL-25377

Light Water Reactor Sustainability Research and Development

Mechanical Properties of Model Cast Austenitic Stainless Steels after Thermal Aging for 1500 Hours

Cast Stainless Steel Aging (LW-16OR0402152)

April 2016

U.S. Depart of Energy

Office of Nuclear Energy

Department of Energy/Office of Nuclear Energy

LWR Sustainability R&D

Cast Stainless Steels Aging (WP#: LW-16OR040215)

Mechanical Properties of Model Cast Austenitic Stainless Steels after Thermal Aging for 1500 Hours

by

Thak Sang Byun

Nicole R. Overman

Timothy G. Lach

Pacific Northwest National Laboratory

operated by

Battelle

for the

U.S. Department of Energy

under contract DE-AC05-76RL01830

TABLE OF CONTENTS

LIST OF TABLES AND FIGURES

MECHANICAL PROPERTIES OF MODEL CAST AUSTENITIC STAINLESS STEELS AFTER THERMAL AGING FOR 1500 HOURS

T.S. Byun, N. R. Overman, T.G. Lach
Nuclear Sciences Division, Pacific Northwest National Laboratory, Richland, WA 99352

ABSTRACT

This report presents mechanical property degradation in the model CASS alloys – CF3, CF3M, CF8, and CF8M – after thermal aging at 290–400°C for 1500 hours. The 1500 hour aging is the shortest-term aging planned in the work package, aiming to evaluate an intermediately-aged status of the CASS materials before aging effects became saturated or reached an over-aged status. The uniaxial tensile test and Charpy impact test data comprise the key datasets used to discuss the effects of thermal aging in the following sections.

The tensile test results indicated that the 1500 hour thermal aging has caused similarly small softening or negligible change in strength, regardless of the differences in chemistry and aging temperature. Both the yield stress (YS) and the ultimate tensile strength (UTS) of CF3, CF8, and CF8M were slightly lowered by the 1500 hour aging, while CF3M retained its strength after the aging treatment. Such aging-insensitive behavior of strength is clearly contrary to the impact energy change showing substantial degradation by the same aging treatment. The small reduction in strength from the 1500 hour aging also simultaneously resulted in a reduction of ductility. Both the uniform elongation (UE) and the total elongation (TE) measured at or above room temperature were reduced by 20–30% in the aging temperature region (290–400°C), expect for a few cases showing more than 50% reduction at room temperature.

The impact energy datasets were analyzed to obtain transition parameters using a four-parameter hyperbolic tangent function and a least square regression technique for curve fitting. The analysis indicated that the effect of thermal aging on transition parameters was not consistent for the four CASS alloys. The reduction of the upper shelf energy was most substantial in CF3 while the shift of ductile-brittle transition region was largest in CF3M. The upper shelf energy (USE) measurements of CF3, CF3M and CF8M were reduced by 43–49% after the 400°C aging, while CF8 showed much less reduction of ~35% after the same aging treatment. This lowest reduction of USE measured in CF8 might be due to having the least δ-ferrite content (5.5%).

The most substantial but gradual shift of the ductile-brittle transition temperature (DBTT) was observed in CF3M with a maximum ΔDBTT of +118°C after the 400°C aging, which has the highest δ-ferrite content of ~12%. Among the four model alloys, the CF8 alloy showed the highest resilience to the DBTT shift, as the ΔDBTT in CF8 was only +17°C after aging. Additionally, to avoid the adverse effect in DBTT behavior (i.e., negative ΔDBTT), the 41J-transition temperature (T_{41J}) has been evaluated using the same hyperbolic tangent curve fitting. The parameter T_{41J} seemed to describe the aging effects more consistently for CASS materials: no decrease of T_{41J} was found after the 1500 hour thermal aging; all four model alloys display gradual shift of ΔT_{41J}; the aging-induced property degradation was measured more sensitively.

1. INTRODUCTION

Cast austenitic stainless steel (CASS) materials are used for numerous nuclear power plant components, including the massive primary coolant piping system. The aging degradation of these components is a major concern in the extended operation of light water reactors (LWRs) not only because the aging phenomena beyond the reactor operating experiences are not fully understood, but also because replacement of such massive components would be prohibitively expensive [1,2]. The integrity assessment for an extended service with existing CASS components will require a widely expanded knowledge base than the current understanding. Therefore, the ongoing research, Cast Stainless Steel Aging, aims to expand scientific understanding on thermal-aging induced degradation phenomena, and ultimately, to provide knowledge-based conclusive prediction for the integrity of the cast austenitic stainless steel (CASS) components of LWR power plants during the service life extended up to and beyond 60 years [3].

The CASS materials are typically graded by their chemistries and fabrication processes [4-6], and most CASS materials used in nuclear power plants have a duplex structure with austenitic (γ) and ferritic (δ) phases. The most common cast alloy grades include the CF family with nominally ~19% Cr and ~10% Ni with 3–30% δ-ferrite, such as the A351-CF3 and A351-CF8 series, with the CF3, CF3A, CF3M, CF8, CF8A, and CF8M being the most prominent variants [1-3,7-14]. The amount of δ-ferrite phase is a critical factor in the mechanical properties after aging, as significant aging degradation is usually associated with high δ-ferrite content, in particular, with > 20% ferrite, where a near-complete contiguity of ferrite can be achieved [7,15,16]. After a long-term service, any cast microstructure containing a significant amount (>20%) of δ-ferrite can become susceptible to the thermally-induced embrittlement in the reactor operating temperature range 280–340°C [1,2,7-9]. Some earlier investigations based on accelerated aging [7-13] have suggested that the thermal embrittlement can occur in cast stainless steel components during the common reactor design lifetime of 40 years, although a complete embrittlement (or zero ductility) above room temperature has not been observed in the CASS components in LWRs.

It is known that the degree of aging degradation in a CASS alloy depends on the chemistry and processing route of the alloy [7-14], because these determine the amount and distribution of δ-ferrite and small precipitates. The low carbon CF3 steels were generally more resistant to the thermal embrittlement than other alloys, while the Mo–bearing, high carbon CF8M steels are among the least embrittlement-resistant alloys. Primary brittle fracture mechanism observed in a thermally embrittled duplex stainless steel is cleavage initiation at ferrite followed by propagation through separation of ferrite-austenite phase boundary. This cracking mechanism could be caused or enhanced by various microstructural changes during thermal aging, such as formation of a Cr–rich α'-phase through the spinodal decomposition of δ-ferrite, precipitation of G-phase and $M_{23}C_6$ carbide, and additional precipitation and growth of carbides and nitrides at ferrite-austenite phase boundaries [7-14,17-26]. In the austenite matrix, on the other hand, thermal aging induces various precipitations but usually causes a negligible to moderate effect on the properties of the phase [9-12]. Precipitation kinetics are relatively slow in the stable austenite phase, and austenite itself retains significant ductility, and therefore the property change – the effect on toughness, in particular – is less pronounced in austenite phase.

In the LWRS R&D project, four model alloys, CF3, CF3M, CF8, and CF8M, have been

thermally aged, along with other CASS materials including four CASS materials from the Electrical Power Research Institute (EPRI) and two wrought stainless steels, for more than a year as of today. Mechanical tests including uniaxial tests and Charpy impact tests at 22–400°C were performed for the model alloys after thermal aging at 290–400°C for the shortest-term of 1500 hours. This report presents the results of mechanical testing for the four model alloys, which includes the following major contents:

(a) Tensile test results are discussed with a focus on the effect of different aging temperatures on the tensile strength and ductility parameters.

(b) The temperature-transition characteristics of impact energy datasets were analyzed using a four-parameter hyperbolic tangent function and a curve fitting method. Key temperature-transition parameters, including the upper shelf energy (USE), ductile-brittle transition temperature (DBTT), and the 41J-transition temperature (T_{41J}), were obtained directly from test data or through curve fitting analyses, and used to display and discuss the degree of degradation by the 1500 hour thermal aging.

(c) The sensitivity of mechanical property parameters to thermal aging was discussed as some parameters, such as tensile strength, displayed much smaller percentage change than others such as the ductile-brittle transition temperatures.

(d) Discussion will be also made for the influential factors in the aging degradation of model CASS alloys. The volume fraction of δ-ferrite and the contents of C and N were the key factors considered to explain the different responses of four model alloys to the same thermal aging treatment.

2. MODEL CAST AUSTENITIC STAINLESS STEELS

2.1. Chemical composition

Four (4) model CASS alloys (CF3, CF3M, CF8, and CF8M) have been produced for systematic study on thermal aging effects. Although a large variety of cast stainless steels have been used in nuclear power plants; as reactor models and alloy selections have evolved with the year of construction, the most commonly used CASS alloys include the four alloys and their variants such as CF3A, CF8A, and CPF8M [2,7-13] (note: A-anneal, M-molybdenum doped, and P-piping). It is thought, therefore, that those four selected CASS grades can represent the vast majority of CASS alloys used in LWR power plants. Listed in Table 1 are the detailed chemistry data obtained for the model alloys.

Table 1. Chemistries of model cast austenitic stainless steels in wt.% or in ppm (for C, S, O and N)

Grade (*)	Fe	Cr	Ni	Mn	Mo	Si	Cu	Co	V	P	C	S	O	N
CF3 (304L)	Bal.	19.17	8.11	1.44	0.34	0.99	0.41	0.18	0.07	0.029	262	324	204	1020
CF3M (316L)	Bal.	19.28	9.81	1.14	2.30	1.22	0.28	0.15	0.05	0.033	284	253	224	838
CF8 (304)	Bal.	18.72	8.91	1.10	0.29	1.27	0.29	0.15	0.05	0.026	665	376	161	606
CF8M (316)	Bal.	18.52	10.38	0.65	2.33	1.02	0.33	0.17	0.06	0.031	433	243	207	1020

*Chemistry specification [6]. Data produced by Dirats Laboratories in Westfield, MA.

2.2. Austenite-ferrite duplex microstructure of model alloys

SEM-EDS maps for key alloy elements (Cr, Fe, Mo, Ni, and Si) were taken to reveal the characteristic austenite-ferrite duplex microstructure of CASS alloys and elemental partitioning between the two constituent phases are displayed in Figure 1 to 4. The EDS maps, in which a brighter color indicates higher content of the element, show elemental partitioning between austenite and ferrite phases. As expected, the ferrite-stabilizing elements (Fe, Cr, and Mo) are enriched in ferrite while Ni favors austenite phase. Using the strong partitioning elements, Cr in ferrite and Ni in austenite, phase volume fractions can be easily measured in the maps by using the distribution of those elements. Si seems to be slightly enriched in ferrite but not obvious in most regions. Mo-enrichment in ferrite is obvious in CF3M and CF8M alloys only, and Fe is slightly enriched in austenite in all model alloys.

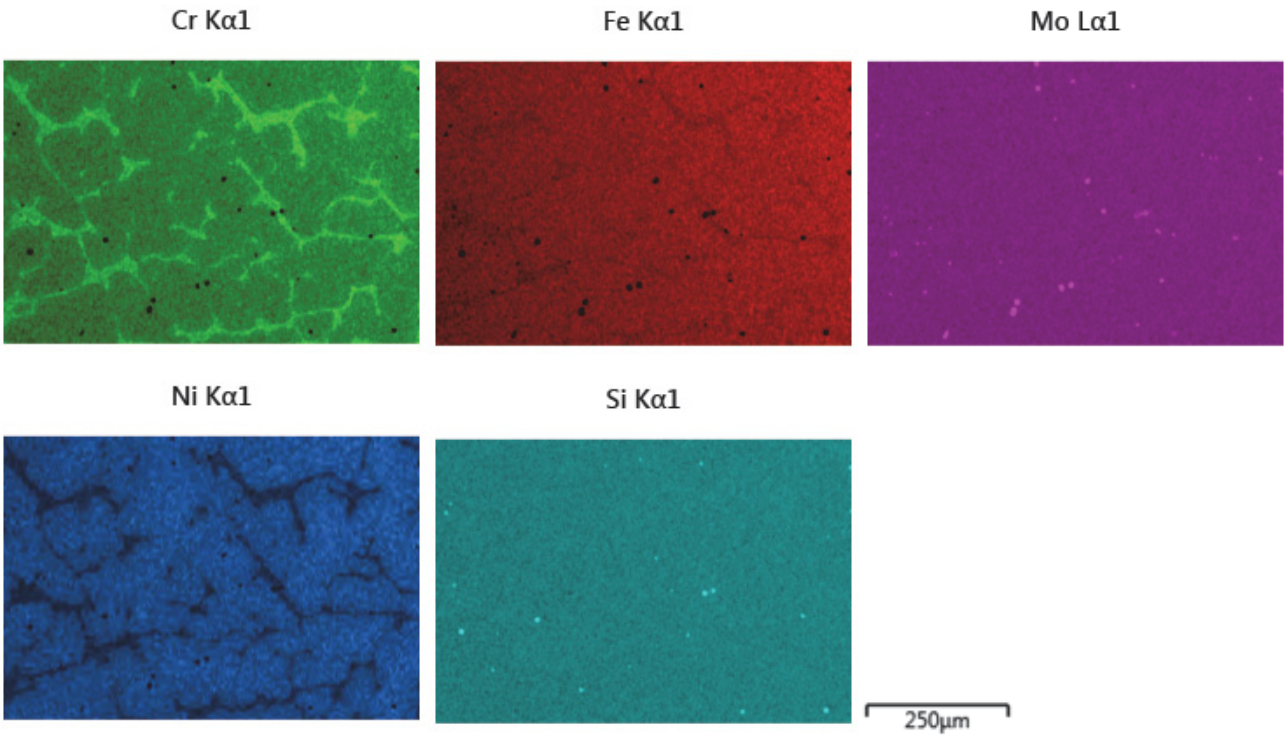

Figure 1. The SEM-EDS maps of CF3 alloy showing γ-δ duplex microstructure and elemental partitioning. The austenite (γ)-phase is matrix and lighter color indicates higher concentration.

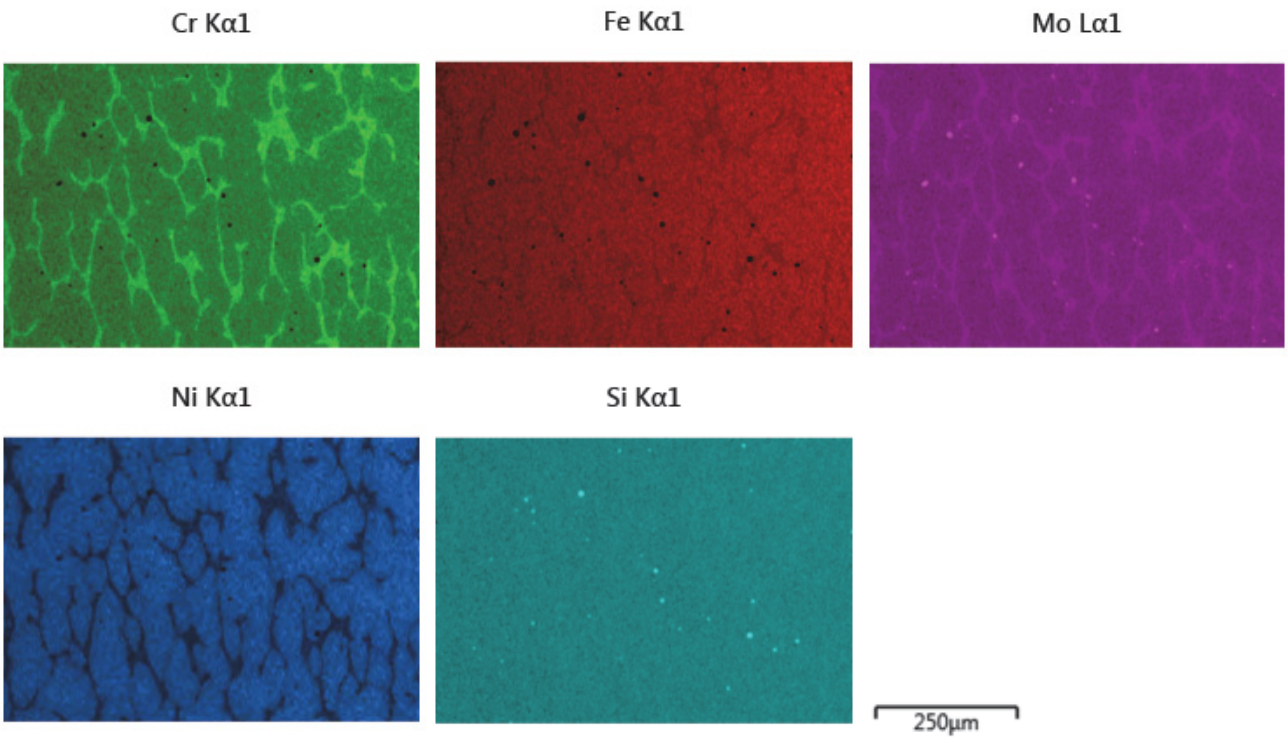

Figure 2. The SEM-EDS maps of CF3M alloy showing γ-δ duplex microstructure and elemental partitioning.

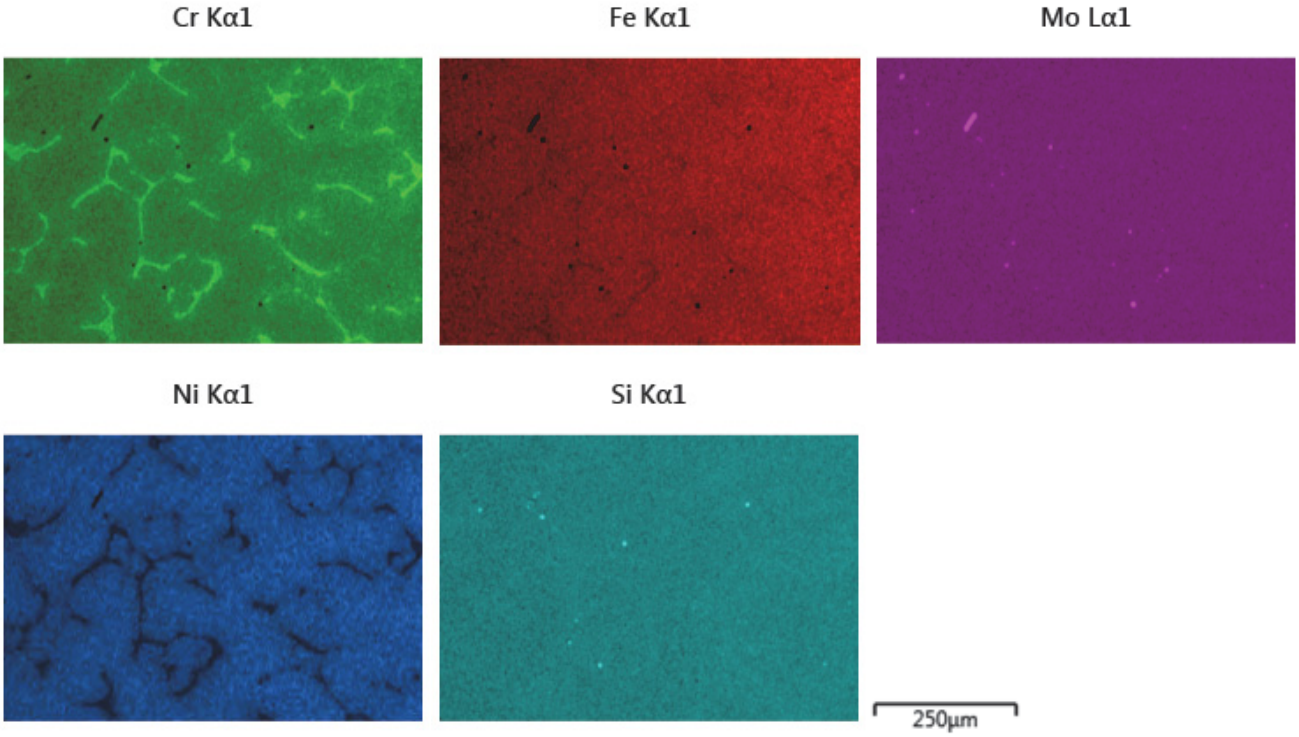

Figure 3. The SEM-EDS maps of CF8 alloy showing γ-δ duplex microstructure and elemental partitioning.

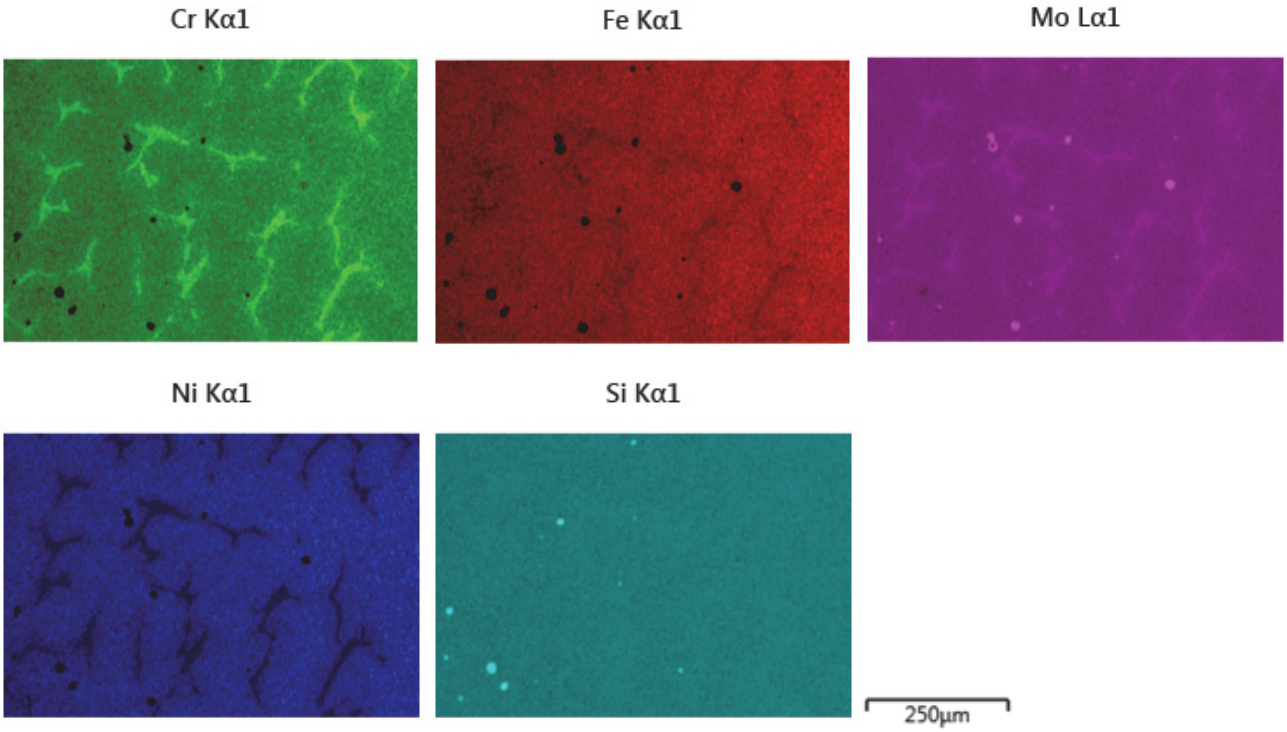

Figure 4. The SEM-EDS maps of CF8M alloy showing γ-δ duplex microstructure and elemental partitioning.

Both optical and scanning electron microscopies have been used to observe phase morphologies and measure volume fractions; the δ-ferrite volume fraction data of the model CASS alloys are summarized in Table 2. The CF3M alloy has the highest volume fraction average of ~12%, which is followed by CF3 with 9.2%. The CF8 and CF8M contain relatively low δ-ferrite contents, 5.5 and 7.9%, respectively. In CASS alloys, the chemical composition and cooling rate determine their microstructure after casting, in particular, determining the volume fractions of ferrite (δ) and austenite (γ) phases. The δ-ferrite content can vary widely with the thermal history of casting process since the cooling rate on passing the ferrite formation area in the phase diagram might determine the total exposure time for ferrite formation. The nuclear grade CASS alloys, CF3 and CF3M, for example, can contain 3 to 30% ferrite in an austenite matrix depending on the cooling rate [1]. In the same processing route, the amount of ferrite-stabilizing elements in the alloy may determine the ferrite volume fraction. In general, the CF8 grade alloys contain only about 10% ferrite, while the CF3 alloys typically have higher amounts of ferrite of 10-20%. It is well known that the amount of δ-ferrite is a critical factor in the aging process because the aging degradation is usually more significant with higher ferrite content. The δ-ferrite phase will experience spinodal decomposition to α' and α phases, and ultimately embrittlement, in particular, with > 20% ferrite where a near-complete contiguity of ferrite can be achieved [7,15,16].

Table 2. Volume fraction of δ-ferrite in the model CASS alloys (in %)

CASS Grade	SEM-1	SEM-2	SEM-3	Optical-1	Average	Stand. Dev.
CF3	11.8	5.1	8.2	11.8	**9.2**	3.23
CF3M	15.0	17.5	7.2	7.9	**11.9**	5.13
CF8	5.6	3.7	6.0	6.7	**5.5**	1.28
CF8M	5.9	7	7.2	11.6	**7.9**	2.52

3. STRENGTH AND DUCTILITY AFTER AGING FOR 1500 HOURS

3.1. Effect of aging on strength

To measure thermal aging effect on strength and ductility, tensile tests were carried out at room temperature (RT) to 400°C for the alloys aged at 290, 330, 360, and 400°C for 1500 hours. The tensile specimens were SS-3 dog-bone type flat specimens with the gage section dimensions of 7.62 mm in length × 0.76 mm in thickness × 1.52 mm in width, and were tested at a displacement rate of 0.5 mm/min. In Figures 5 and 6, the yield strength (YS) and ultimate tensile strength (UTS) after thermal aging are plotted against test temperature, in comparison with the baseline (non-aged alloy) data which were previously reported [27].

A general temperature dependence of strength observed in the model alloys (CF3, CF3M, CF8 and CF8M) before aging was that the strength parameters such as YS and UTS decreased with test temperature up to 290°C and showed little change in the aging temperature range of 290-400°C. It is commonly observed in Figures 5 and 6 that the 1500 hour-long thermal aging has not changed the temperature dependence of strength in these alloys. Such a little change in the temperature dependence of strength may indicate that the strengthening mechanisms being operated in the test temperature range remain unchanged after such a short-term aging.

Further, it is observed that the 1500 hour thermal aging has not induced any recognizable difference among the strength data for different aging temperatures. Both the YS and UTS data after aging at different temperatures are contained within narrow bands: the band width of UTS for each alloy is approximately 100 MPa and is roughly twice that of YS (~50 MPa) because of the similar ratio (~2) between UTS and YS. This strength behavior without evident dependence on aging temperature might indicate that the microstructural mechanisms inducing strength change during aging in 290-400°C range are either negligible or remained complementing each other.

For all the model alloys, the thermal aging for 1500 hours has caused an overall small change in strength, regardless of the differences in chemistry and aging temperature. In detail, both the YS and the UTS of CF3, CF8, and CF8M alloys were slightly lowered by the 1500 hour aging, while the CF3M alloy retained its strength after the aging treatment. Such a reduction of strength might indicate that some softening mechanisms such as ferrite decomposition, dislocation annihilation, reduction in solid solution effect, and stress relaxation have over-compensated the hardening amount by precipitation. This relatively aging-insensitive aspect in strength is clearly contrary to the impact energy behavior to be described in the next sections.

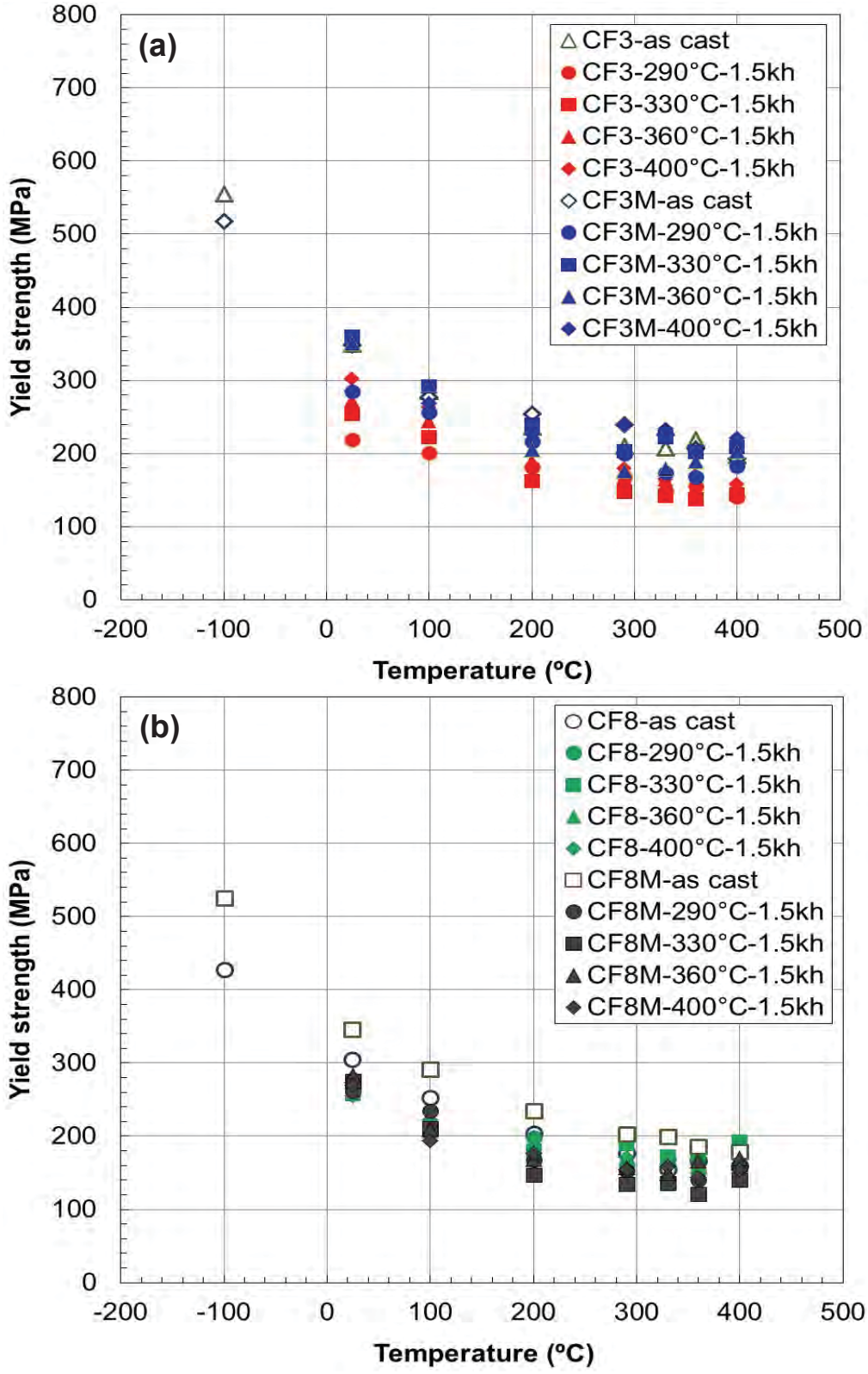

Figure 5. Effect of 1500 hour thermal aging on yield strength (YS) in (a) CF3 and CF3M and (b) CF8 and CF8M alloys

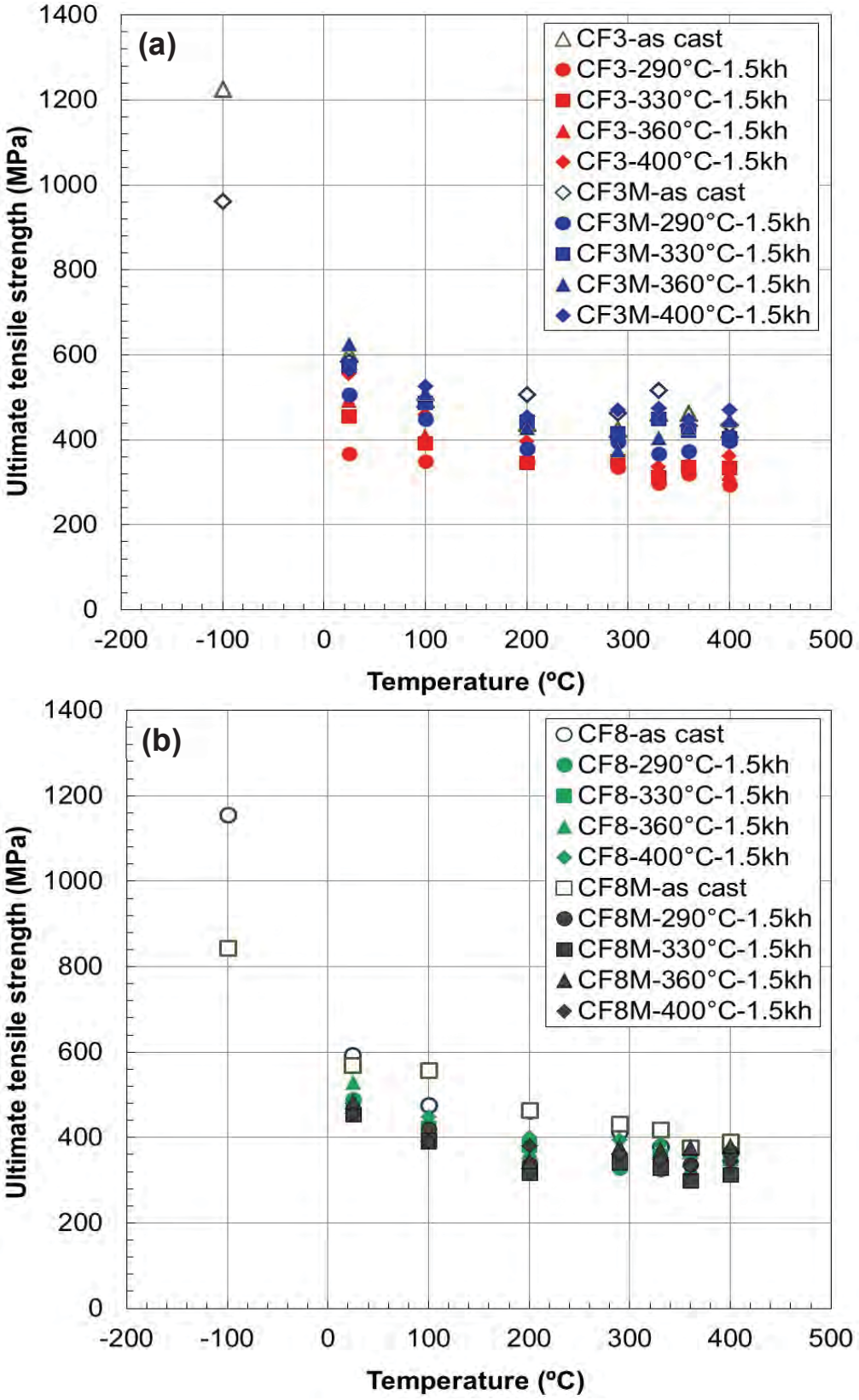

Figure 6. Effect of 1500 hour thermal aging on ultimate tensile strength (UTS) in (a) CF3 and CF3M and (b) CF8 and CF8M alloys

3.2. Effect of aging on ductility

The uniform and total elongations (UE and TE) for the aged and non-aged model CASS alloys are displayed in Figures 7 and 8. It is commonly found in the datasets for non-aged alloys that the uniform and total elongations decrease with test temperature before they become nearly temperature independent in the aging temperature region (290-400^{o}C). This test temperature dependence of ductility is very similar to that of strength although the large scattering in elongation data seems to be too large to discern any occurrence of temperature dependence within the aging temperature range. The ductility datasets for aged alloys show that such temperature dependence has been retained after the 1500 hour aging; however, it has become less steep in the lower temperature region up to 200°C, which resulted in relatively large reduction in ductility in the lower temperature region and relatively muted temperature dependence in a wide test temperature range above 200°C. A comparison between the data of aged and non-aged alloys also shows that both UE and TE at or above room temperature were significantly reduced after aging. A few elongation data after aging present more than 50% reduction at room temperature, while the ductility reduction is typically 20-30% in the 290-400^{o}C region, except for the CF8 alloy that showed much less reduction overall. It is pointed out that the model alloys after aging retain high uniform ductility > ~20% over the whole test temperature range and relatively small necking ductility (TE-UE) of about 5% in average, which is close to the average value for non-aged alloys of 6%. The higher % reduction in ductility at lower temperatures, the majority of which occurred in uniform ductility, may indicate that the plastic glide becomes less linear after aging [28,29].

As observed in the strength and ductility curves in Figures 5 to 8, the 1500 hour aging has resulted in a simultaneous reduction of strength and ductility. This phenomenon might be explained in association with the characteristic deformation mechanism of austenitic stainless steels: highly linear slip. It is well known the extraordinarily high uniform ductility and work hardening capability of these alloys originate primarily from their linear dislocation glide, which can generate higher internal stress and resulting strain hardening rate when compared to random dislocation glide [28,29]. This deformation mechanism can explain the temperature dependence of tensile properties; a characteristic behavior observed in austenite-dominant materials only is that both ductility and strength decrease with test temperature. Such simultaneous decrease of strength and ductility can be explained by the fact that the degree of linearity in slip band formation should decrease with increasing deformation temperature as the cross-slip of dislocations can occur more easily at higher temperatures. In thermal aging, the small reduction of strength will reduce the tendency for linear or twinning deformation that can decrease strain-hardening rate, and thus, uniform ductility. Further, some microstructural processes during aging treatment, such as segregation and partitioning of solid solution elements, may increase stacking fault energy, which usually reduces the tendency for linear dislocation glide. More random glide will eventually reduce both ductility and strength.

The strength and ductility datasets in Figures 5 to 8 also indicate that the effect of 1500 hour aging on tensile properties is not strongly dependent on aging temperature. Similar to the strength behavior discussed earlier, the strength and ductility data of both aged and non-aged alloys distribute within similar band widths, though the band widths in the ductility data are much wider in percent than those of the strength data. This result again proves that the tensile deformation is not sensitive to the aging temperature, at least after the shortest aging (1500 hour) in the present research.

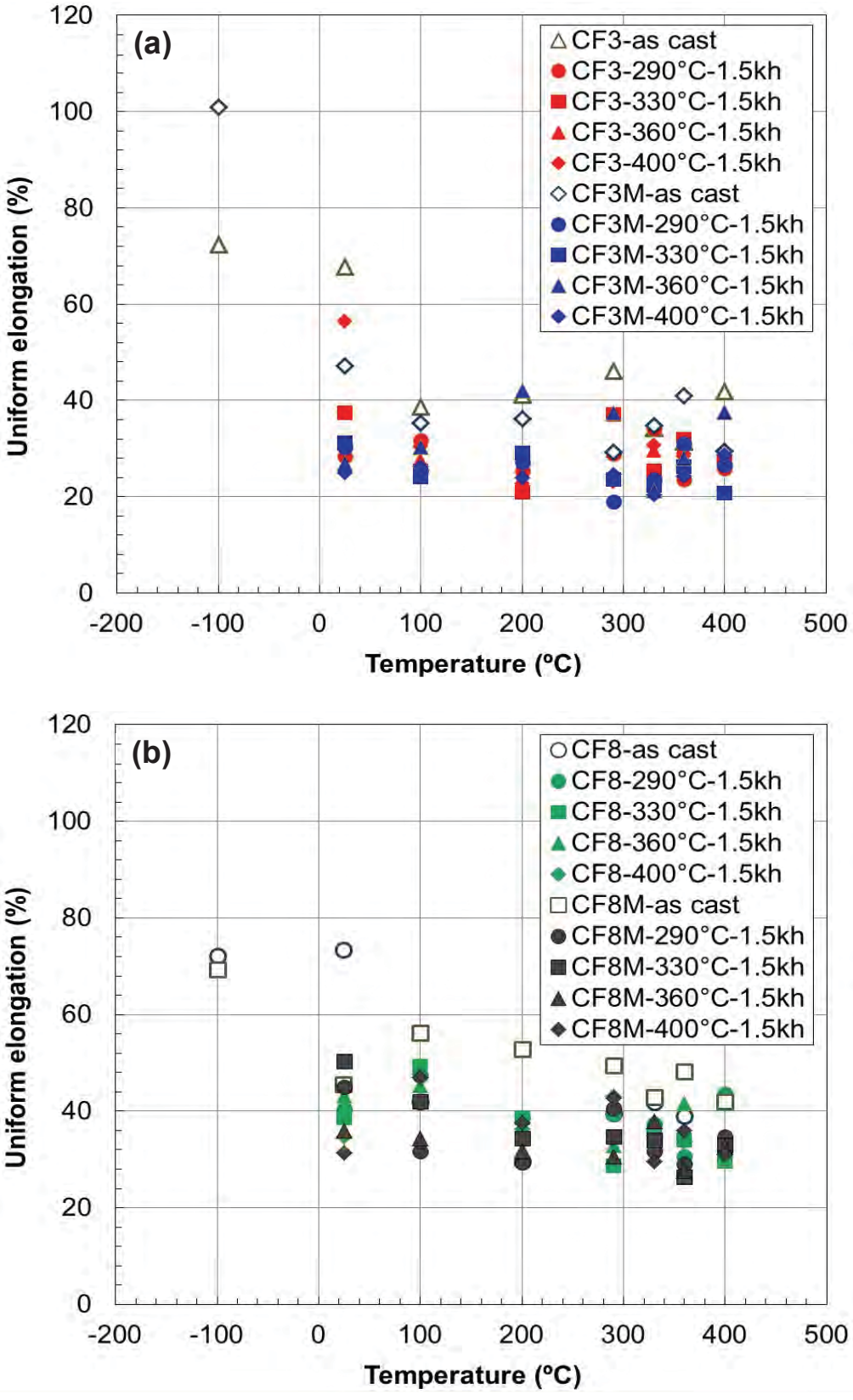

Figure 7. Effect of 1500 hour thermal aging on uniform elongation (UE) in (a) CF3 and CF3M and (b) CF8 and CF8M alloys

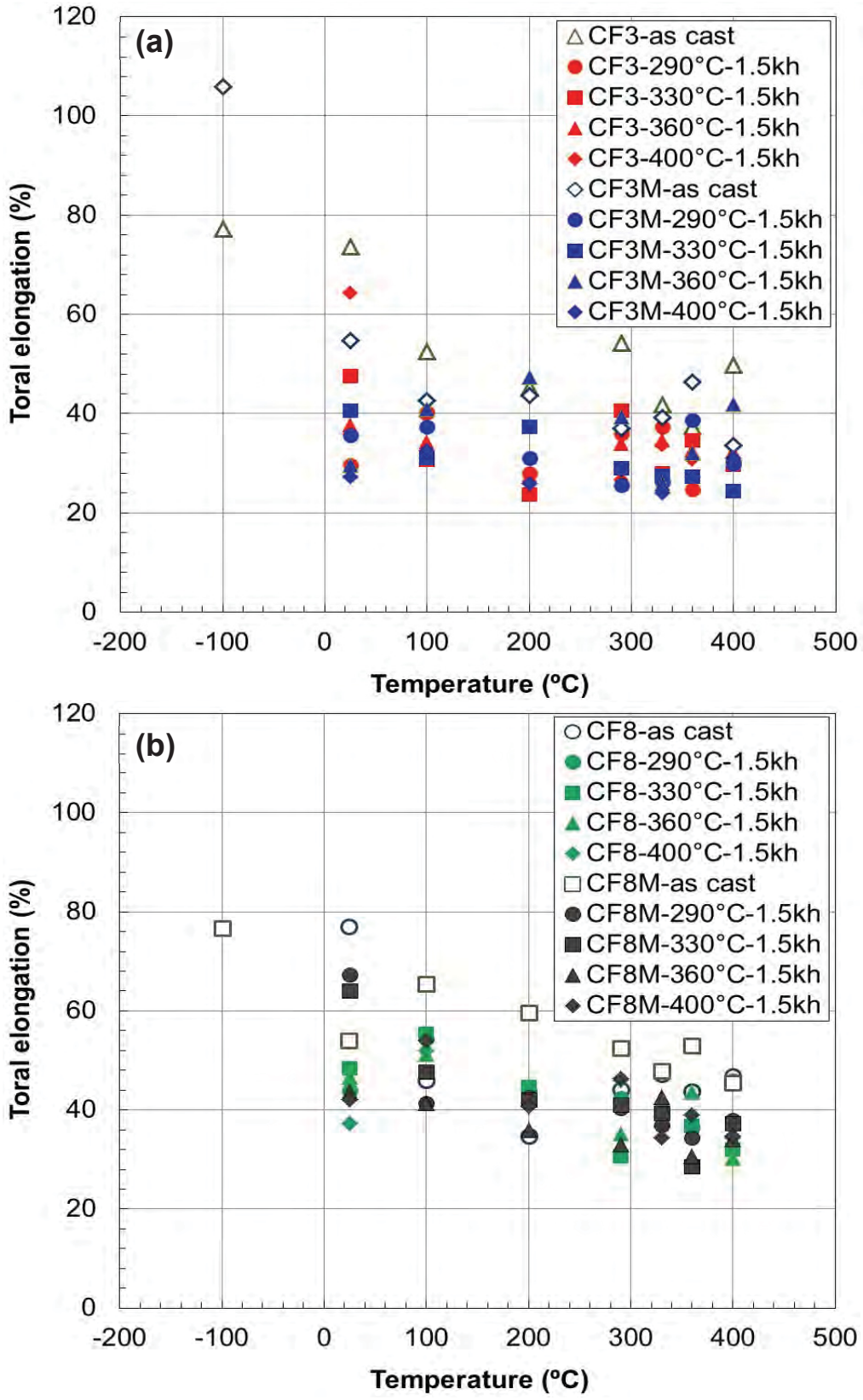

Figure 8. Effect of 1500 hour thermal aging on total elongation (TE) in (a) CF3 and CF3M and (b) CF8 and CF8M alloys

4. IMPACT ENERGY AFTER AGING FOR 1500 HOUR

4.1. Hyperbolic tangent curve analysis

For each aging condition of the four model CASS alloys (CF3, CF8, CF3M, and CF8M), an impact (or absorbed) energy versus temperature curve were obtained from the standard Charpy specimens (10 mm × 10 mm × 25 mm bend bar with a 2 mm deep 45° notch) in a wide temperature range including impact energy transition region. The impact testing was performed in a 300 J capacity Charpy impact tester, and for each condition 12-13 tests were performed to construct a complete temperature transition curve. Curve fitting analysis for the impact energy datasets was performed to obtain the temperature transition parameters using a four parameter hyperbolic tangent function [30,31]:

$$E(T) = A + B \times \tanh\left(\frac{T-D}{C}\right) \qquad (eq.1)$$

where A is the vertical position of the inflection point, B is the vertical distance between point A and the upper and lower shelves, C is one-half the width of the transition region, and D is the horizontal position of the inflection point. As shown in Figure 9, key transition curve parameters can be defined using these parameters: the value $A+B$ is defined as the upper shelf energy (USE), and A-B is defined as the lower shelf energy (LSE). The parameter D becomes the ductile-brittle transition temperature (DBTT), which is the midpoint temperature in the temperature-transition region. The best fit curves can be found using the ordinary least squares (OLS) regression technique or similar regression methods. In practical analysis the two parameters, the LSE and USE, can be determined by plotting measured absorbed energy data, and therefore the DBTT value is used as an iteration parameter. The LSE can be set at 20 J for stainless steels [32].

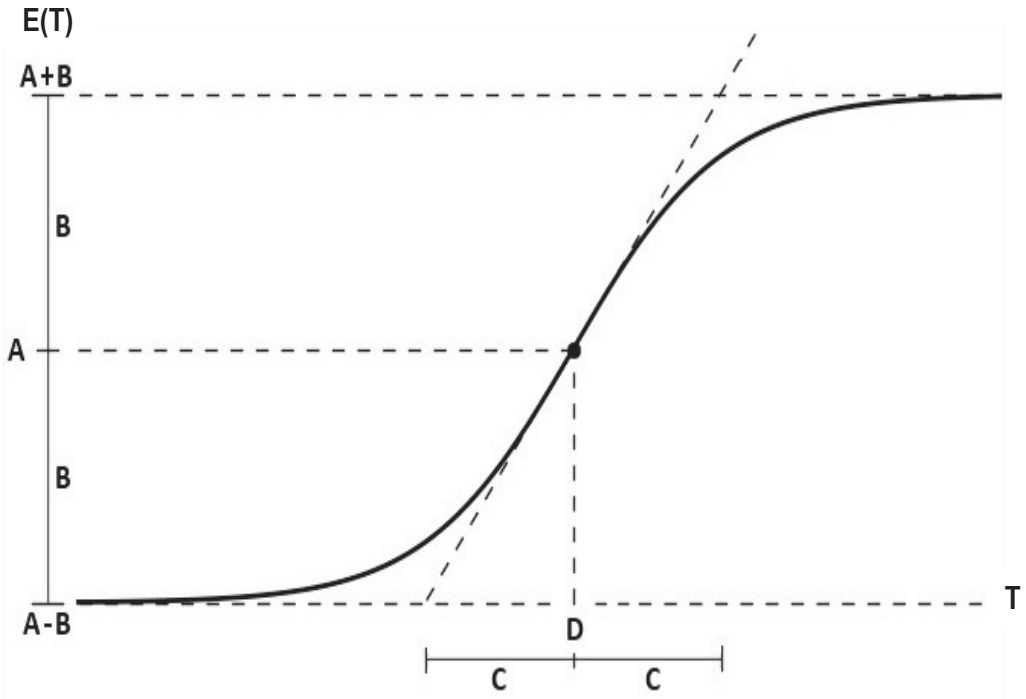

Figure 9. Definition of parameters in the ductile-brittle transition curve.

A drawback of using the symmetrical hyperbolic tangent function is that its application can be often limited to the transition region and its vicinity. As shown in Figure 9, the hyperbolic tangent function asymptotically approaches their shelf values as test temperature decreases and increases in lower and upper shelf regions, respectively. In most of the ferritic and austenitic steels, however, the impact energy (or toughness) measurement decreases with test temperature after passing a maximum plateau. In the present analysis, the average of a few absorbed energies at the plateau around the maximum was used as the USE.

Another drawback we can encounter when we use the traditional DBTT definition is that a dramatic reduction of USE can cause a net effect of moving DBTT lower and a negative shift of DBTT can be measured even if the test material has been degraded. Examples will be shown in a later section. A nil-ductility temperature (NDT) can be used to avoid this effect; therefore the 41J (30 lb-ft) index temperature, T_{41J}, is additionally calculated from the same fitted curves, and the results are presented in the last section.

4.2. Temperature-transition curves

The impact energy datasets and corresponding fitted hyperbolic tangent curves are presented in Figure 10 for CF3 and CF3M alloys and in Figure 11 for CF8 and CF8M. First, it is noted that the impact energy curves of non-aged CASS alloys do not reach their lower shelves as the measured absorbed energies at the lowest test (liquid nitrogen) temperature were much higher than the expected lower shelf value of 20 J. It is also observed that in some of the datasets for aged alloys the measured impact energy decreases with test temperature above their maximum energy temperatures.

Each of the model alloys demonstrates a significant reduction of upper shelf energy and a large shift of transition temperature after the 1500 hour aging. It is observed, however, that their detailed temperature-transition behaviors are not uniform in the model alloys. For instance, a comparison of Figures 10(b) and 11(a) indicates that the aging-induced changes in the impact energy curves in CF3M and CF8 alloys display different dependences on aging temperature. If measured by the shift of transition region and decrease of impact energy, the CF3M alloy experienced more profound degradation in a short aging term of 1500 hours; Figure 10(b) shows that the CF3M alloy after 400°C aging has a significant shift of the transition region (~120°C shift toward higher temperature), and the upper shelf energy is reduced by more than 40%. The CF8 alloy shows similar degree of impact energy reduction, but its transition region shift after 400°C aging is much smaller (< 50 °C). Another notable difference between these two alloys is that the shift of the transition region and the reduction of impact energy gradually with aging temperature in CF3M, but they are less sensitive to the aging temperature in CF8.

In addition, the CASS materials with higher molybdenum contents showed more significant degradation in the impact energy transition behavior: the 2.3% Mo-doped alloys (CF3M and CF8M) showed more significant reduction of impact energy and larger shift of transition temperature region, compared to the CF3 and CF8 alloys. This should be because the molybdenum, which is a ferrite former, has helped to form higher amounts of δ-ferrite in those Mo-doped alloys during casting process. Table 2 confirms that the δ-ferrite volume fractions are more than 2% higher in the Mo-doped alloys. These alloys also showed different degradation behaviors: although both CF3M and CF8M showed significant reduction of impact energy over all test temperatures, the dependence on aging temperature was much less obvious in CF8M.

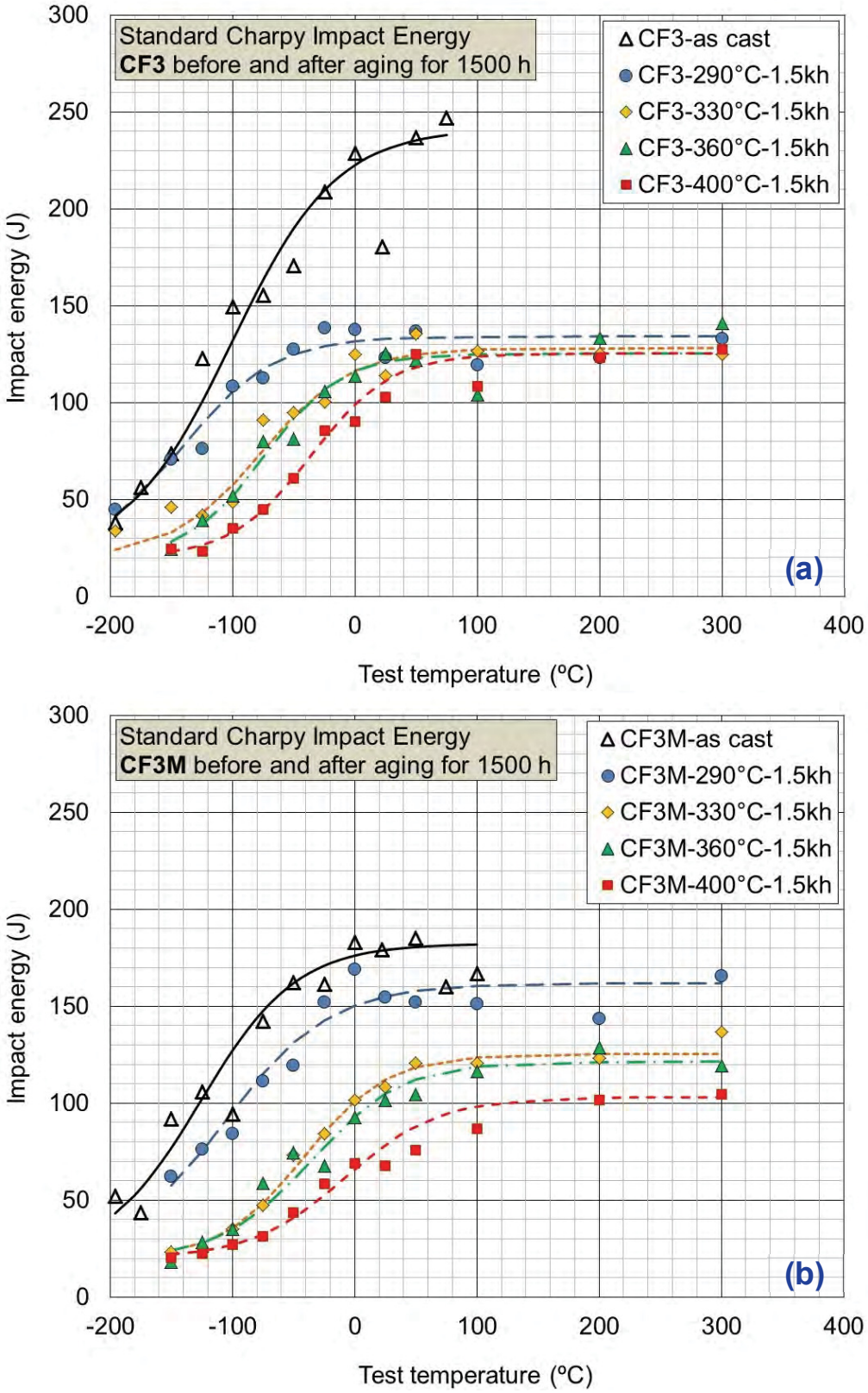

Figure 10. Temperature-transition curves of Charpy impact energy for (a) CF3 alloy and (b) C3M alloy after aging for 1500 hours.

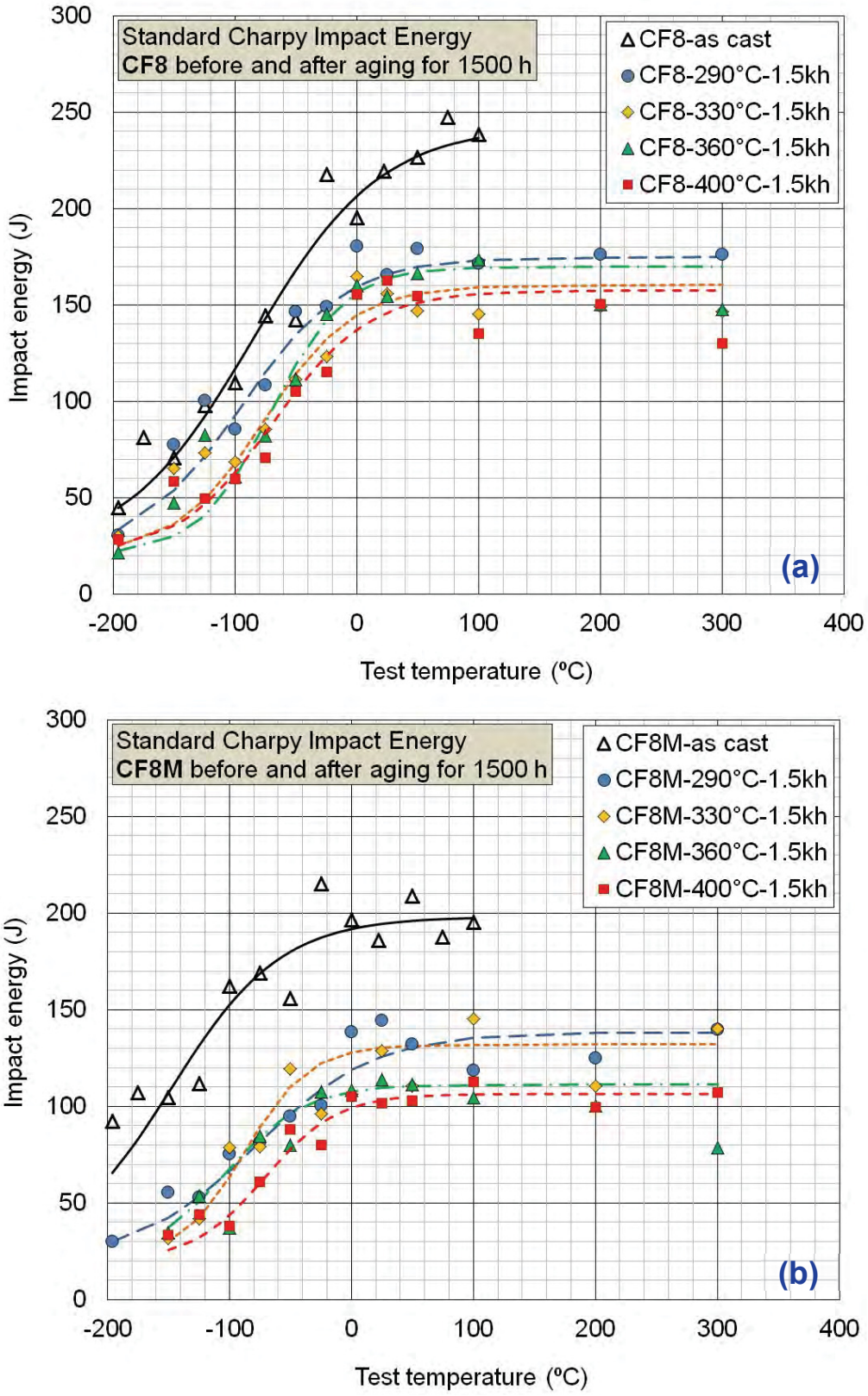

Figure 11. Temperature-transition curves of Charpy impact energy for (a) CF8 alloy and (b) CF8M alloy after aging for 1500 hours.

4.3. Aging effect on upper shelf energy

The experimental USE data used in transition curve analysis are compared altogether in Figure 12, where the columns with red border are those of the non-aged CASS alloys. As discussed in the above section, the temperature-transition curve behaviors indicate that the effects of thermal aging on different parameters in the CASS alloys do not occur in a uniform manner; the reduction of USE is the most abrupt and substantial in CF3, and the smallest in CF8. Further, the USE after aging has the least dependence on aging temperature in CF3 but much clearer dependence in the Mo-doped CF3M and CF8M alloys. It is also observed that, despite significant reduction in USE for all aged model alloys, no alloy actually showed embrittlement in the upper shelf region, which is near or above room temperature for all cases. The lowest USE measured after 1500 hour aging was still higher than 100 J.

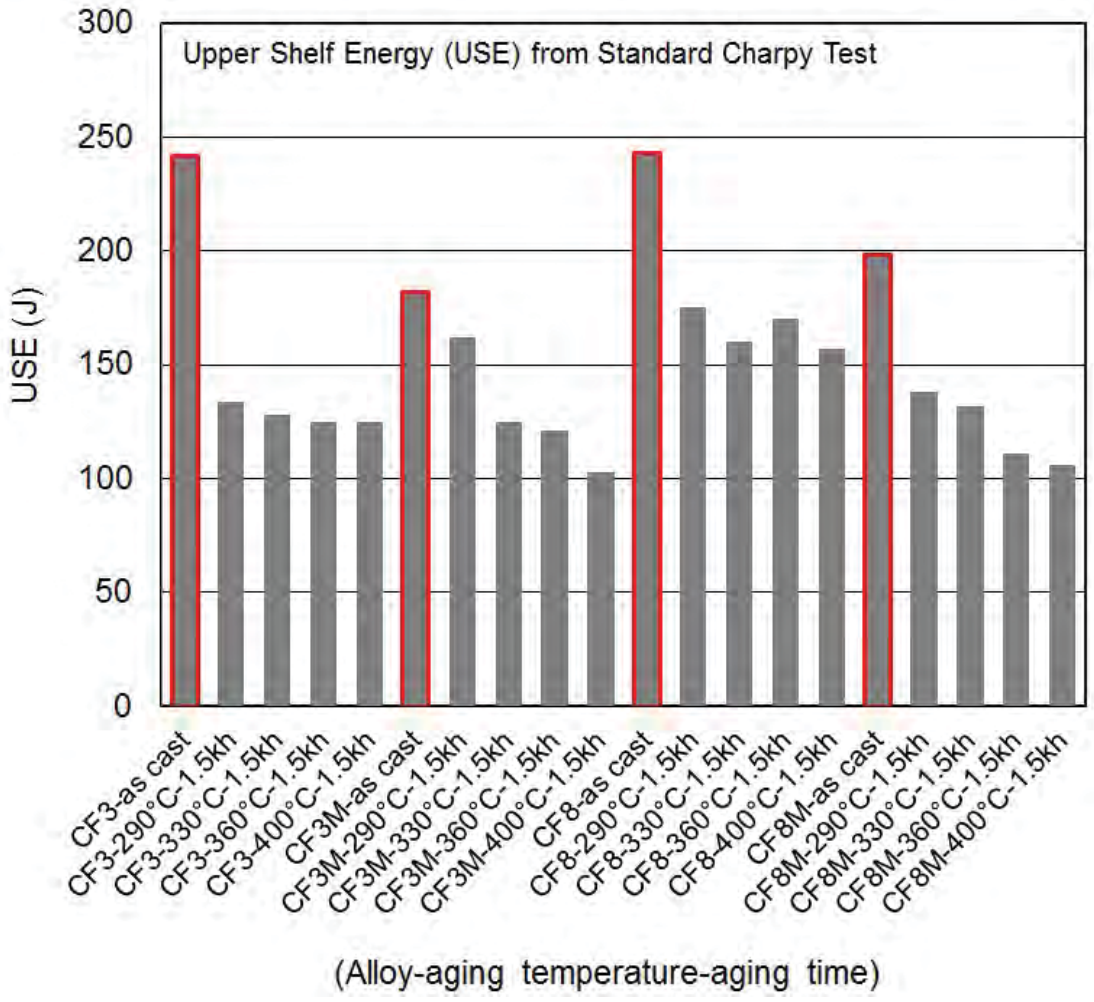

Figure 12. Reduction of upper shelf energy after 1500 hour aging

It was predicted that the USE after aging at the highest aging temperature of 400°C would be the lowest for each alloy. Before aging, USE was relatively high for non-aged CF3 and CF8 alloys (~240 J), and slightly lower for CF3M and CF8M alloys (182 J and 198 J, respectively).

The USE measurements of CF3, CF3M and CF8M were reduced by 43-49% after the 400°C aging, while CF8 showed much smaller reduction of ~35% after the same aging. This lowest reduction of USE measured in CF8 may be due to it having the lowest δ-ferrite content (5.5%) among the model alloys; which is consistent with it having the smallest shift in transition-temperature, as discussed below.

4.4. Aging effect on transition temperatures: DBTT and T_{41J}

Figure 13 compares the DBTT data measured from the four model alloys before and after 1500 hour aging. As indicated in the change of temperature-transition curve, the most substantial and gradual shift of DBTT is observed in CF3M; the DBTT of -126 °C in as-cast condition increased to -106, -41, -35, and -8°C after aging at 290, 330, 360, and 400°C, respectively. The maximum shift of DBTT (ΔDBTT) is +118°C. Similar behavior, i.e., a gradual shift of DBTT with aging temperature, is observed in CF3 and CF8 alloys but to a much lesser degree in the amount of shift. Among the four model alloys, the CF8 alloy seems to show the highest resilience to the DBTT shift, as the DBTT change in CF8 was relatively moderate and the maximum ΔDBTT was only +17°C. The DBTT data of CF8M show that the 1500 hour aging has shifted its DBTT by similar amounts of 45-77°C, despite different aging temperatures.

Overall, the DBTT data demonstrates that its shift is dependent on alloy and aging temperature, with relatively stronger aging-temperature dependence found in CF3 and CF3M compared to CF8 and CF8M. It is noted, however, that the aging-temperature dependence of DBTT is not quite the same as that of USE, where relatively clearer dependence is found in CF3M and CF8M. Further, as discussed earlier, the tensile strength and ductility data indicated little aging-temperature dependence, and to a much lesser degree, aging-induced property degradation. These indicate that the degree of property deterioration is highly dependent on the measured parameter. In general, a mechanical property parameter involving a notch or crack might be more sensitive to thermal aging.

An abnormal behavior observed in the DBTT data, Figure 13, is the negative shift of DBTT: the evaluated ΔDBTTs are -40 and -9°C, respectively, for the CF3 and CF8 alloys after 1500 hour aging at the lowest temperature of 290°C. It is believed that this negative shift is associated with the pure mathematical definition of DBTT, which is the midpoint temperature of USE and LSE. That is, the upper shelf region was significantly reduced at the lowest temperature (290°C aging), and such a large USE reduction with a small shift of the transition region resulted in the negative shift of DBTT. It can be concluded, therefore, that the property degradation measured by the change of DBTT may not be conservative enough to reflect the true aging effect. A parameter to avoid such an adverse effect should be the one that is defined at single impact energy such as the transition temperature at an impact energy of 41J (T_{41J}).

In Figure 14, no decrease of T_{41J} is found after the 1500 hour thermal aging. More importantly, all four model alloys display, approximately, a gradual and larger shift of the NDT temperature (ΔT_{41J}). Further, the difference among the alloys before aging is less profound; for instance, the difference of T_{41J} between non-aged CF8 and CF8M alloys is only 33°C, while it is 62°C in DBTT data. Note that this parameter is more representative of nil-ductility transition (NDT) temperature, and for a highly ductile alloy, can be lower than the lowest testing temperature as it has to be determined with extrapolation. Overall, it is seen that the T_{41J} data, when compared to the DBTT data, can measure property degradation more sensitively and

reasonably. For the CF3, CF3M, CF8, and CF8M alloys after 400°C aging, the ΔT_{41J} values were measured to be 115, 151, 69, and 134°C, respectively, which correspond to the ΔDBTT values of 65, 118, 17, and 77 °C.

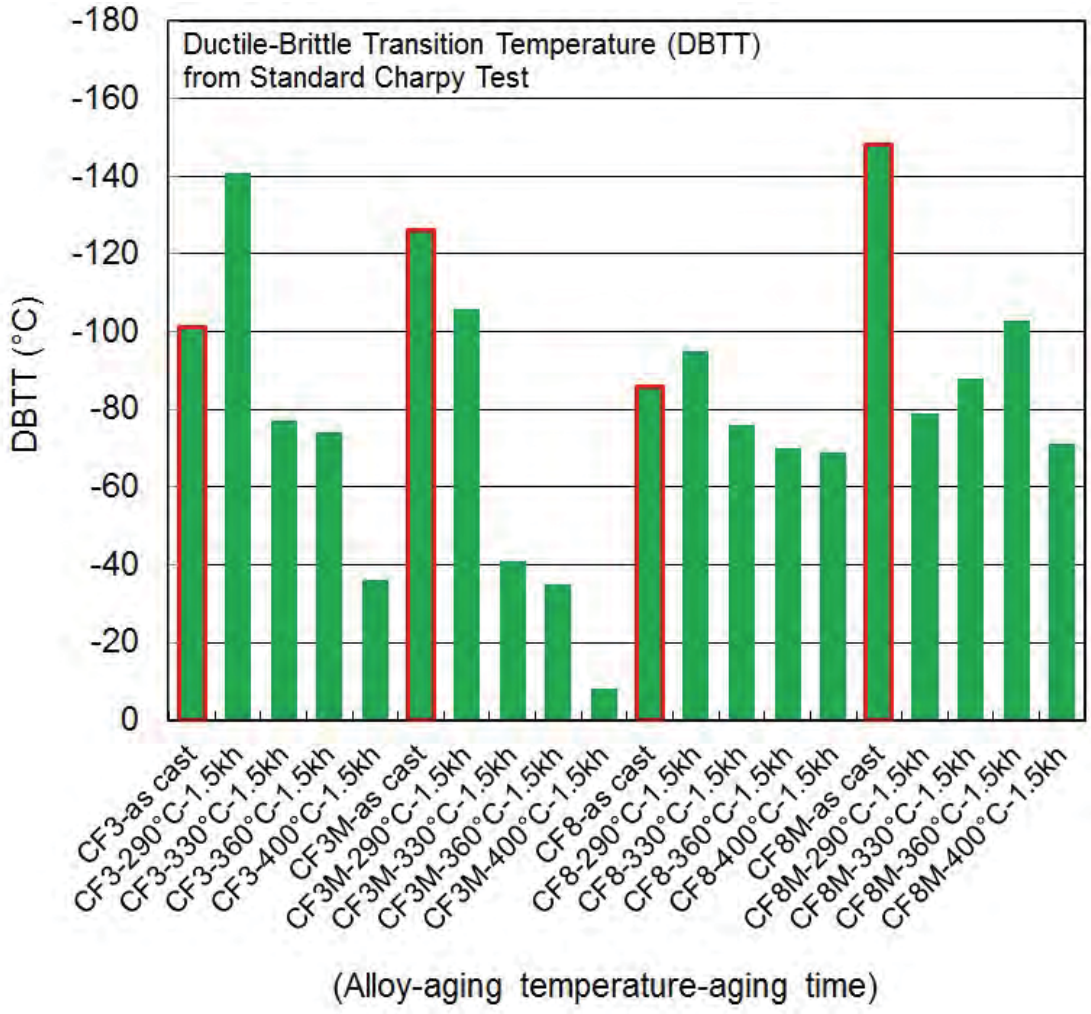

Figure 13. Effect of 1500 hour aging on ductile-brittle transition temperature (DBTT)

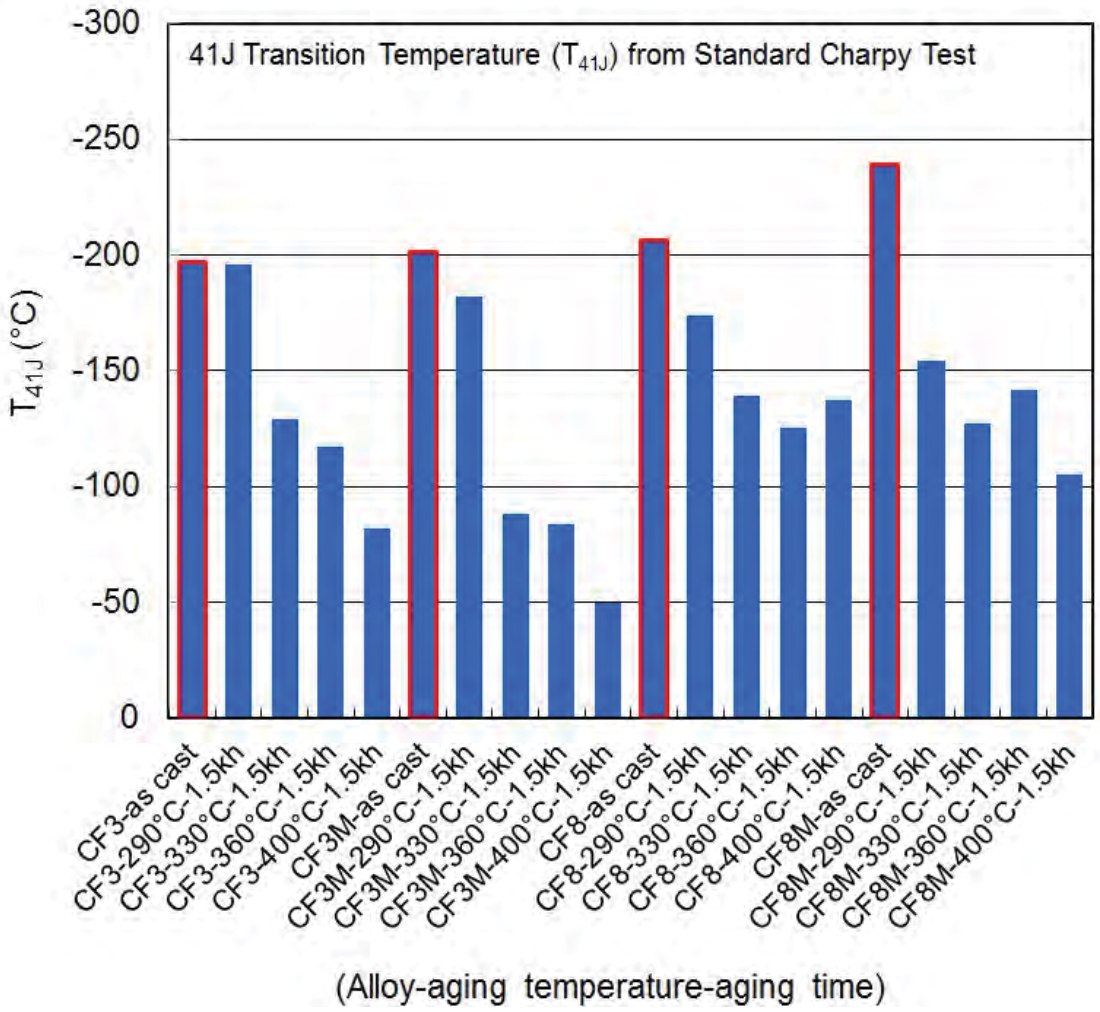

Figure 14. Effect of 1500 hour aging on the 41J-transition (index) temperature (T_{41J})

5. DISCUSSION

5.1. Degree of property degradation by 1500 hour aging

An aging mechanism with higher activation energy generally causes faster embrittlement, and materials with the same chemical composition but different processing routes show different kinetics of embrittlement [11]. An accurate prediction of mechanical property degradation based on indirect measurements or generalized input has not been performed previously because it is highly dependent on detailed microstructural processes. For instance, the aging time at 400°C measured at the same reduction of impact energy in different heats varied by more than two orders of magnitude [11]. The primary embrittlement mechanism, spinodal decomposition of δ-ferrite, should have higher activation energy because of the short range and fast characteristics of the process [9,12,17,18, 21-24]. The strengthening in ferrite is caused primarily by spinodal decomposition of ferrite to form the Cr–rich α'-phase, and consequently, the kinetics of thermal embrittlement should be controlled by the size and spacing of α'-phase. However, the CASS

materials with low activation energy and slow embrittlement at 400°C showed G-phase precipitation after aging, and steels with high activation energy and fast embrittlement at 400°C did not contain G-phase [7-13,19]. Often, the weld alloys with similar compositions show lower activation energies, 65 kJ/mole, for example, and much slower property degradation when compared to commercial CASS alloys [32].

Mechanical property degradation at an aging temperature (T) can be approximately gaged by an aging parameter (P) which is based on the thermodynamic activation processes following the Arrhenius type kinetics with average activation energy (Q) [12]. It is assumed that the resulting microstructure and chemical redistribution are fully responsible for the property degradation measured by mechanical testing. The parameter P at given aging time (t in h) and aging temperature (T in K) is given as

$$\mathrm{P(T)} = log_{10}\langle t \times \exp[\left(-\frac{Q}{R}\right)\left(\frac{1}{T}-\frac{1}{T_0}\right)]\rangle \qquad \text{(eq. 2)}$$

where T_0 is a reference temperature (e.g., 320°C).

If we apply this equation to the 1500 hour aging, the parameter P will be calculated to be 2.1, 3.5, 4.4, and 5.5 for aging temperatures 290, 330, 360, and 400°C, respectively. A typical value of 220 kJ/mole was used for Q in this calculation. The highest P value of 5.5, therefore, is similar to the P range 5.5–5.8 which was evaluated for 40 to 80 years of aging at 320°C. This demonstrates that the 1500 hour aging at 400°C can approximately simulate the degree of degradation for the designed or extended service life of CASS components. Meanwhile, the aging treatments at lower temperatures help to simulate intermediate level degradations for the CASS materials.

As shown in Figures 10-14, the degree of impact property change is significant even after the short aging time of 1500 hours, which would indicate that the major degradation mechanism is the traditional spinodal decomposition in δ-ferrite. The biggest concern for an extended-term service of CASS components has been their susceptibility to the thermal aging-induced embrittlement at reactor operating temperatures ranging from 280 to 340°C [7-13]. A complete embrittlement may be defined as the material status at the lower shelf fracture parameter value in room temperature to operation temperature range. If assuming that the activation energy based analysis is valid, the experimental and analytical results discussed above (see the worst case – CF3M data after 400°C aging) don't predict any complete embrittlement in CASSs occurring within the current design lifetime; although the thermal degradation is still the biggest concern, and the aging time of 1500 hours may be too short to yield confirmatory results. This prediction may be contrary to the conclusions of earlier investigations that have suggested that the thermal embrittlement can occur in cast stainless steel components during the common reactor design lifetime of 40 years [7-13]. It rather agrees with the past experiences that complete embrittlement has not been observed in the CASS alloys thermally aged in LWR conditions.

5.2. Influential factors in aging degradation in model alloys

The degree of aging embrittlement in a CASS depends on many factors such as the grade or chemistry, processing route, and impurity level of the alloy. The primary brittle fracture mechanism observed in the thermally-embrittled duplex stainless steels was the cleavage cracking initiating at the decomposed ferrite and propagating along the ferrite-austenite phase

boundary. Further, the main microstructural mechanisms of thermal aging at <500°C are associated with the phase change in the δ-ferrite: formation of a Cr–rich α'-phase and Fe-rich α-phase through spinodal decomposition and precipitation of G-phase (Ni, Si rich) particles and $M_{23}C_6$ carbides, and precipitation and/or growth of carbides and nitrides at ferrite-austenite phase boundaries [7-13,17,18,19-26].

It is recognized that the above degradation and fracture mechanisms are associated with the amount and chemical composition of δ-ferrite. Since the four model alloys have been produced at Stainless Foundry & Engineering (Milwaukee, WI) as 9–12 cm diameter ingots, their cast microstructures were formed in close casting conditions, and therefore the effects of component size and different processing route on non-aged microstructures should be insignificant. Thus, the amount, chemical composition, and morphology of δ-ferrite formed in the four model alloys should be determined primarily by their average chemical compositions. Comparing the measurements of δ-ferrite volume fraction provided in Table 2, it is obvious that the average volume fraction of δ-ferrite in CF3M alloy, ~12%, is the highest average, for which the largest standard deviation was also measured. It is therefore believed that the most profound reduction of USE, and the largest and most gradual shift of transition temperatures – DBTT and $T4_{1J}$ – originate from the highest δ-ferrite content among the four model alloys, which might be helped by the highest amount of ferrite formers (Cr, Mo, and Si).

It is also anticipated that the contents of light elements such as C, N, S, and O can affect the degradation processes in CASS as they can form precipitates and inclusions. The nitrogen content appears to have a weak correlation, if any, with property degradation. That is, the CF3 and CF8M alloys with high N contents > 1000 ppm showed relatively large ΔT_{41J} of 115 and 134°C, respectively, after 400°C aging although its effect seems to be easily overwhelmed by the effects of Mo or δ-ferrite. Meanwhile, the carbon content seems to affect the aging degradation in the opposite way. This may be because the carbon is a strong austenite former, and the effect from more austenite formation (i.e., less δ-ferrite formation) helped by carbon might result in less degradation in properties, compensating any adverse effects such as precipitation of carbides. The CF8 alloy with the highest C content (see Table 1) exhibited the least property degradation among the model alloys. It has been previously shown that the low carbon CF3 (with 304L chemistry) steels were generally more resistant to the thermal embrittlement than other alloys, while the Mo–bearing, high carbon CF8M steels are among the least embrittlement-resistant alloys [7-14]; however, the discussion above indicates that the effect of higher δ-ferrite is too dominate to discern the positive effect of low carbon in the property degradation.

The major alloying elements in CASSs, such as Ni, Mo, and Mn, should accelerate or decelerate the embrittlement process depending on alloy [9]. Without detailed microscopy analyses, however, the roles of those major elements, as well as the detailed behaviors of minor elements, cannot be accurately described.

6. SUMMARY AND CONCLUSION

The CASS materials portfolio in the Cast Stainless Steel Aging project includes four model CASS alloys being aged at 290, 330, 360, and 400°C for more than a year as of April, 2016. The model cast alloys consist of grade CF3, CF3M, CF8, and CF8M, and were selected to represent the vast majority of CASS alloys used in LWR power plants. The shortest-term (1500 hour)

aging of the model alloys has been completed in FY 2015 and characterized in the past few months. The mechanical and microstructural characterization data obtained for the aged and non-aged model CASS alloys were presented in the present report. Uniaxial tensile and Charpy impact test data in the terms of various parameters comprise the key datasets used to discuss the effects of thermal aging after the 1500 hour aging. The discussion focused on the degree of aging degradation in the model alloys and possible influential factors, and the outcomes are summarized as follows:

(1) SEM-EDS maps were taken to reveal the elemental partitioning between the two constituent phases, and those showed strong partitioning of some elements: the ferrite-stabilizing elements (Fe, Cr, and Mo) were enriched in δ-ferrite while Ni favors γ-austenite phase. Mo-enrichment in ferrite was obvious in the Mo-doped CF3M and CF8M alloys only, and Fe was slightly enriched in ferrite in all model alloys.

(2) The 1500 hour thermal aging has caused small softening or negligible change in strength, regardless of the differences in chemistry and aging temperature. Both the YS and the UTS of CF3, CF8, and CF8M alloys were slightly lowered by aging, while the CF3M alloy retained its strength after the aging treatment. The behavior of relatively aging-insensitive strength change is clearly contrary to the impact energy behavior.

(3) The 1500 hour aging has resulted in a simultaneous reduction of strength and ductility. A few UE and TE data after aging presented more than 50% reduction at room temperature, while ductility reduction was generally in 20-30% range in the temperature range 290-400°C, except for the CF8 alloy that showed much less reduction overall.

(4) The USE measurements of CF3, CF3M and CF8M were reduced by 43-49% after the 400°C aging, while CF8 showed much less reduction of ~35% after the same aging. This lowest reduction of USE measured in CF8 may be due it having the lowest δ-ferrite content (5.5%) among the model alloys. It is also observed that, despite the significant reduction in USE, no alloy actually showed embrittlement near or above room temperature and the lowest USE measured after 1500 hour aging was still higher than 100 J.

(5) The most substantial and gradual shift of DBTT was observed in CF3M, which has the highest δ-ferrite content: the DBTT of -126 °C in as-cast condition increased to -106, -41, -35, and -8°C after aging at 290, 330, 360, and 400°C, respectively (maximum ΔDBTT=+118°C). Similarly, a gradual shift of DBTT with aging temperature was observed in CF3 and CF8 alloys but to a much lesser degree. Among the four model alloys, the CF8 alloy showed the highest resilience to the DBTT shift as the ΔDBTT was only +17°C after aging at 400°C.

(6) The parameter T_{41J} proved to describe the aging effects more consistently. No decrease of T_{41J} was found after the 1500 hour thermal aging. All four model alloys display, approximately, a gradual and larger shift of the NDT temperature (ΔT_{41J}). In the T_{41J} data, the difference among the alloys before aging was less profound, and the aging-induced property degradation was measured more sensitively.

(7) The aging degradation was approximately estimated using an aging parameter (P) based on thermodynamic activation processes. The result confirmed that the 1500 hour aging at 400°C can approximately simulate the degree of degradation for the designed or extended service life of CASS components.

(8) The most influential factor that might determine the degree of thermal aging degradation is likely the volume fraction of δ-ferrite because the majority of microstructural degradation and fracture mechanisms occur in δ-ferrite or at ferrite-austenite boundaries. Further, the nitrogen and carbon contents are believed to have only weak but opposite effects in the degradation of impact property.

REFERENCES

1. J.T. Busby, P.G. Oberson, C.E. Carpenter, M. Srinivasan, *Expanded Materials Degradation Assessment (EMDA)-Vol. 2: Aging of Core Internals and Piping Systems,* NUREG/CR-7153, Vol. 2, ORNL/TM-2013/532, October 2014.
2. R. Dyle, *Materials Degradation Matrix and Issue Management Tables Overview-LTO Update* (Presented at the Second Workshop on U.S. Nuclear Power Plant Live Extension, Washington, D.C, 2011).
3. T.S. Byun, J.T. Busby, *Cast Stainless Steel Aging Research Plan,* ORNL/LTR-2012/440, September 2012.
4. ASTM A743/A743M-13, *Standard Specification for Castings, Iron-Chromium, Iron-Chromium-Nickel, Corrosion-Resistant, for General Application*.
5. ASTM A744/A744M-13, *Specification for Castings, Iron-Chromium-Nickel, Corrosion Resistant, for Severe Service*.
6. ASTM A351/A351M-14, *Standard Specification for Castings, Austenitic, for Pressure-Containing Parts.*
7. K. Chopra and A. Sather, *Initial Assessment of the Mechanisms and Significance of Low-Temperature Embrittlement of Cast Stainless Steels in LWR Systems (*NUREG/CR–5385, 1990).
8. Chopra, *Effects of Thermal Aging and Neutron Irradiation on Crack Growth Rate and Fracture Toughness of Cast Stainless Steels and Austenitic Stainless Steel Welds* (NUREG/CR-7185, 2014).
9. K. Chopra, *Estimation of Fracture Toughness of Cast Stainless Steels during Thermal Aging in LWR Systems* (NUREG/CR-4513, 1991).
10. W.F. Michaud, P.T. Toben, W.K. Soppet, and O.K. Chopra, *Tensile-Property Characterization of Thermally Aged Cast Stainless Steels (*NUREG/CR-6142, 1994).
11. H.M. Chung and T R. Leax, *Mater. Sci. Technol.* 6, 249–262 (1990).
12. H.M. Chung, *Evaluation of Aging of Cast Stainless Steel Components* (Presented at ASME Pressure Vessel & Piping Conference, San Diego, CA, 1991).

13. H. M. Chung, *Presented at the American Society for Mechanical Engineers-Material Properties Council Symposium on Plant Life Extension for Nuclear Components* (Honolulu, Hawaii, 1989).

14. T.S. Byun, Y. Yang, N.R. Overman, J.T. Busby, *Thermal Aging Phenomena in Cast Duplex Stainless Steels,* JOM, 68(2) (2016) 507-526.

15. T.S. Byun and I.S. Kim, *J Mater. Sci.* 26, 3917 (1991).

16. T.S. Byun and I.S. Kim, *J Mater. Sci.* 28, 2923 (1993).

17. S. Li, Y.L. Wang, H.L. Zhang, S.X. Li, K. Zheng, F. Xue, X.T. Wang, *J Nucl. Mater.* 433, 41 (2013).

18. M. Murayama, Y. Katayama and K. Hono, *Metall. Mater. Trans. A.* 30A, 345 (1999).

19. T. Sourmail, *Mater. Sci. Tech.* 17, 1 (2001).

20. L.P. Stoter, *J. Mater. Sci.* 16, 1039 (1981).

21. B. Weiss and R. Stickler, *Metal Trans.* 3, 851 (1972).

22. J.E. Spruiell, J.A. Scott, C.S. Ary, and R.L. Hardin, *Metal Trans.* 4, 1533 (1973).

23. J. Charles *Proceedings of Duplex Stainless Steel Conference*, Vol 1 (Les Editions de Physique, Les Ulis Cedex, 1991) pp. 3-48.

24. K.H. Lo, C.H. Shek, J.K.L. Lai, *Mater Sci Eng. R* 65, 39 (2009).

25. P. Hedström, S. Baghsheikhi, P. Liu, J. Odqvist, *Mater. Sci. Eng. A* 534, 552 (2012).

26. C. Pareige, S. Novy, S. Saillet, P. Pareige, *J. Nucl. Mater.* 411, 90 (2011).

27. T. S. Byun and Y. Yang, *Baseline Characterization of Cast Stainless Steels* (ORNL/TM-2014/446, 2014)

28. T.S. Byun, *Acta Materialia,* 51 (2003) 3063–3071.

29. T.S. Byun, N. Hashimoto, K. Farrell, Acta Materialia, 52 (2004) 3889–3899.

30. W. Oldfield, *Curve Fitting Impact Test Data: A Statistical Procedure, ASTM Standardization News,* 3(1 1) (1975) 24-29.

31. K. Yeager, *Nonlinear curve fitting and the Charpy impact test: statistical, mathematical, and physical considerations* (https://www.uakron.edu/dotAsset/2116623.pdf).

32. S.K. Kim, Y.S. Kim, *Estimation of Aging Embrittlement of LWR Primary Pressure Boundary Components,* J. Kor. Nucl. Soc. 30(6) (1998) 609-616.

APPENDIX-PHASE STRUCTURE AND GRAIN ORIENTATION

Scanning electron microscopy (SEM) data for the 4 model alloys in as-cast condition are displayed in this appendix. Images of plain SEM images, phase maps, and inverse pole figure (IPF) maps are provided in the following pages. In IPF maps, each of the corners of the IPF is assigned with a color to form the color scheme (see IPF color Key provided). A reference sample direction is selected and the color assignment is done based on determined crystal orientation and selection viewing direction.

Specimen: CF3 (Block B, Fractured Specimen)

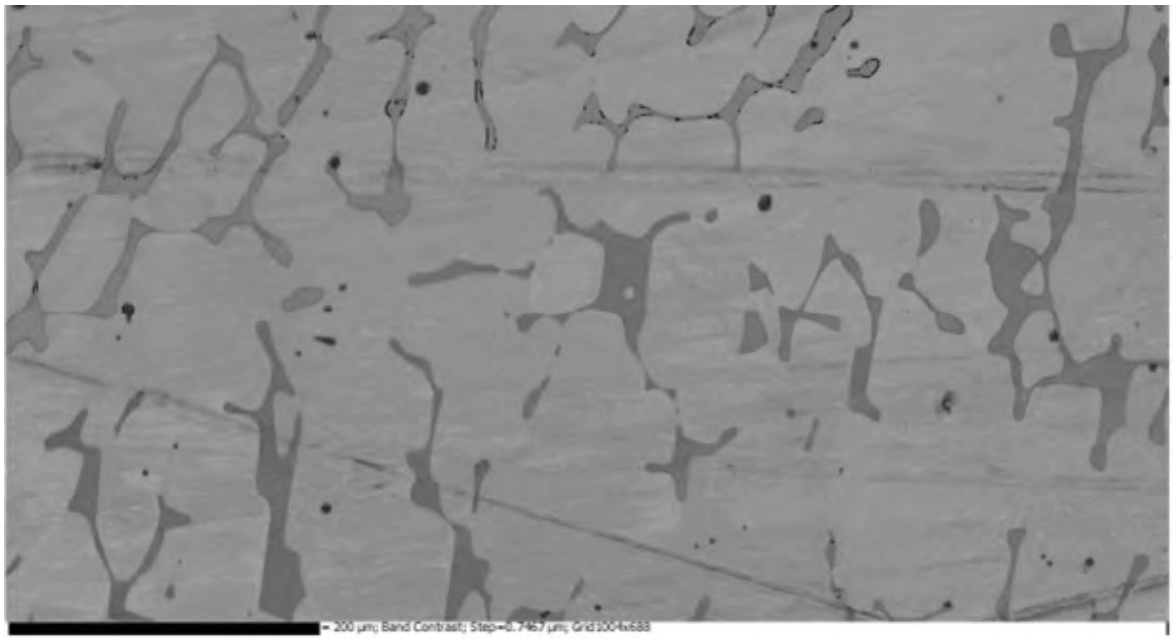

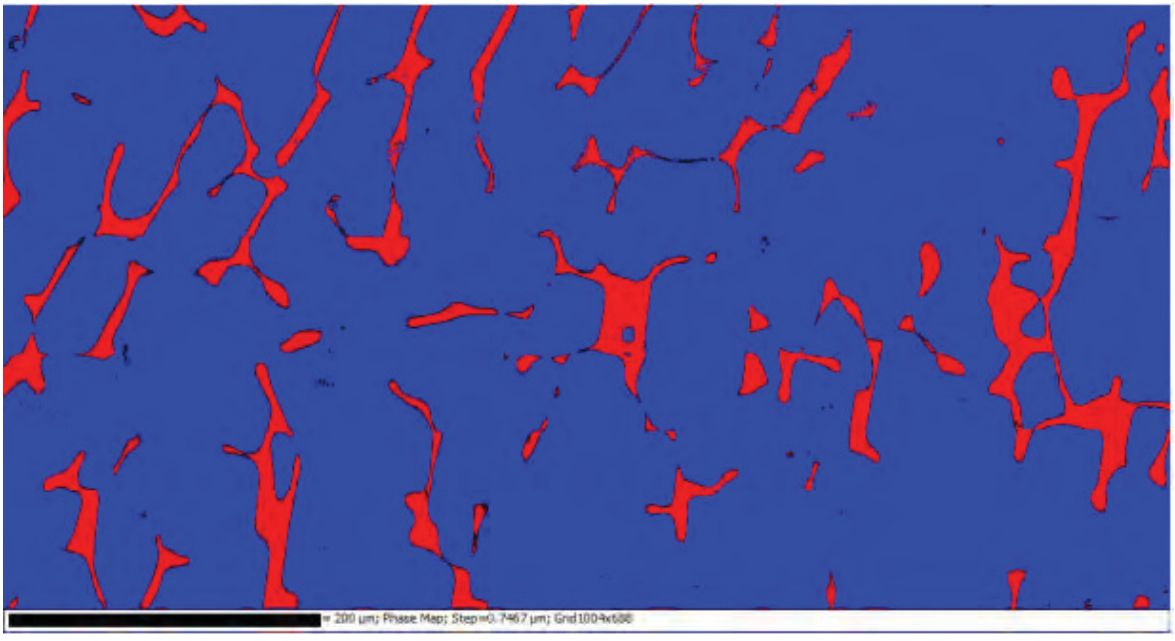

Pattern Quality (top), Phase Map (bottom)

Volume Fraction BCC Phase (red) = 7.2%

IPF-X

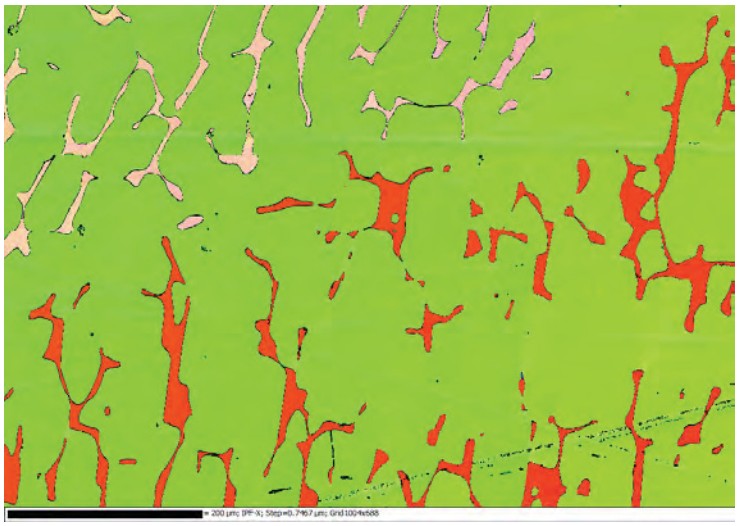

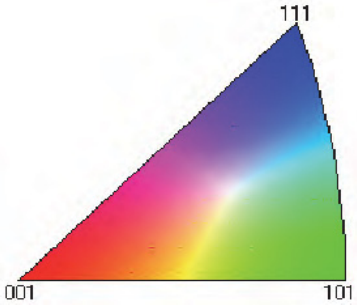

IPF-Y

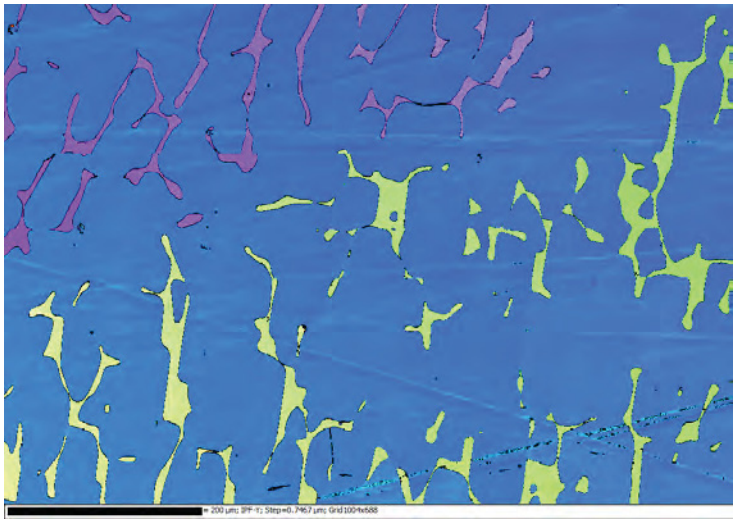

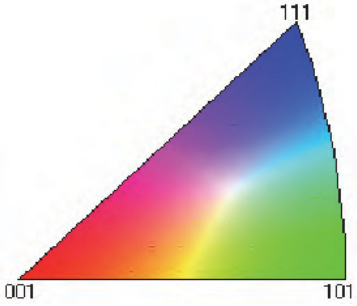

IPF-Z

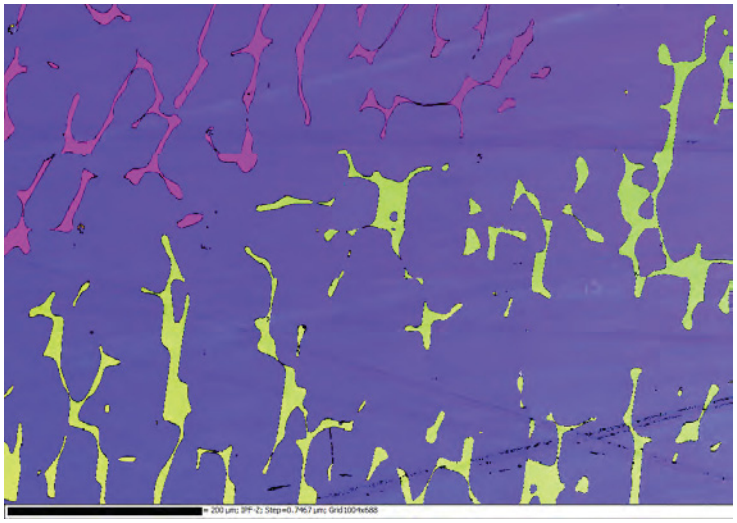

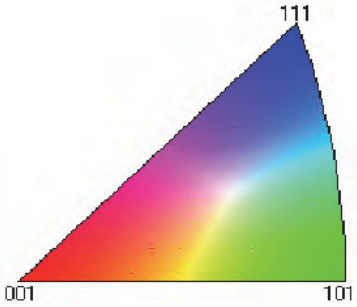

Specimen: CF3M (Block A, Fractured Specimen)

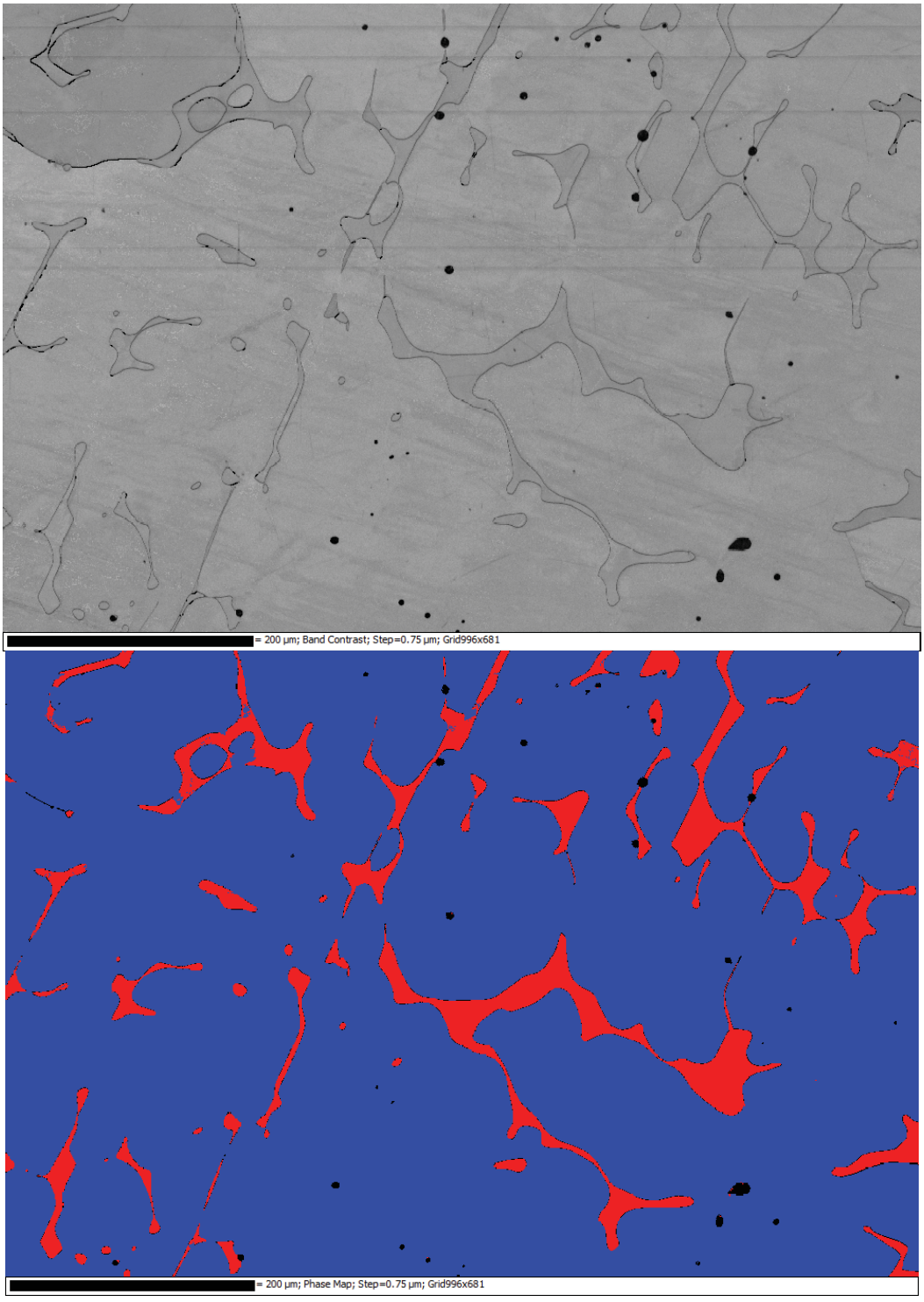

Pattern Quality (top), Phase Map (bottom)

Volume Fraction BCC Phase (red) = 8.2%

IPF-X

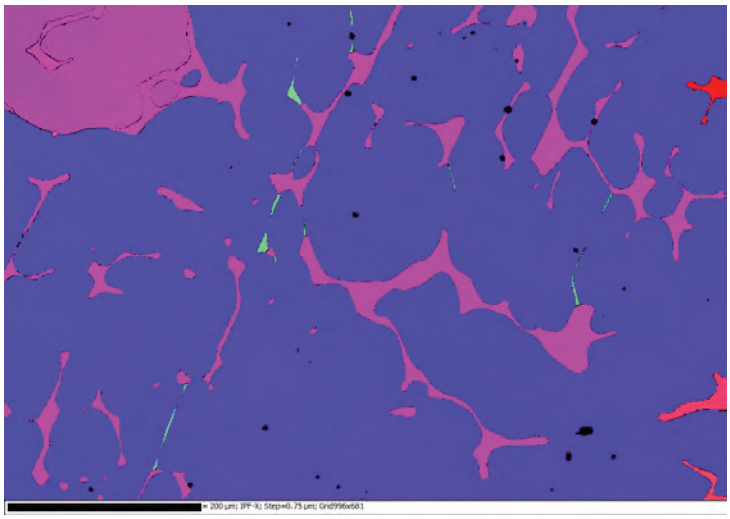

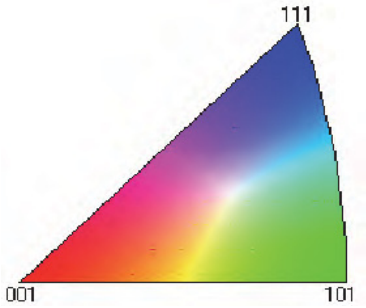

IPF-Y

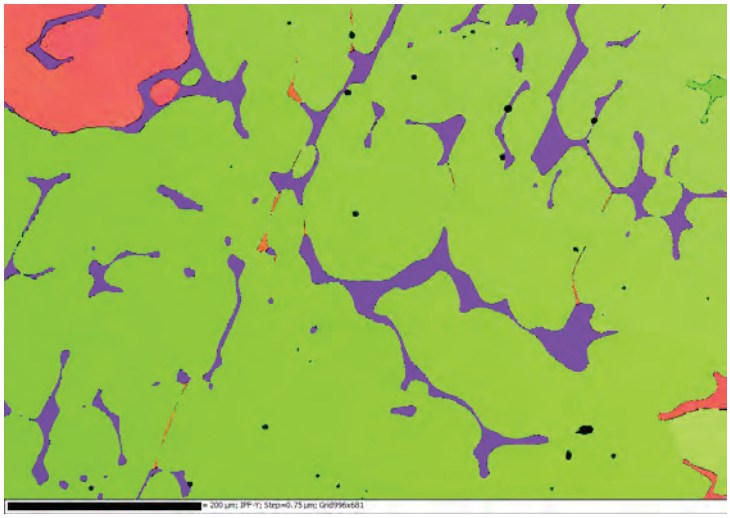

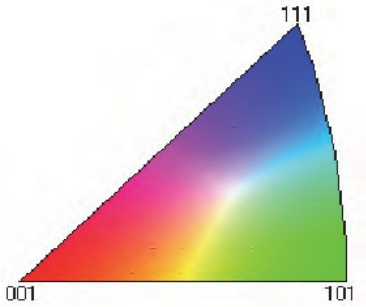

IPF-Z

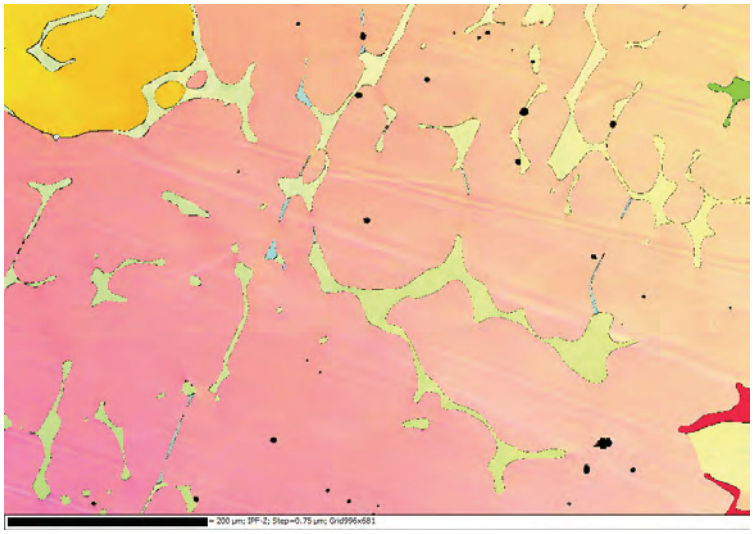

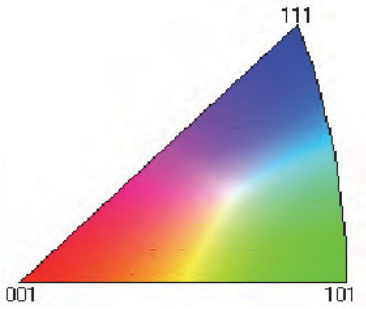

Specimen: CF8 (Block A, Fractured Specimen)

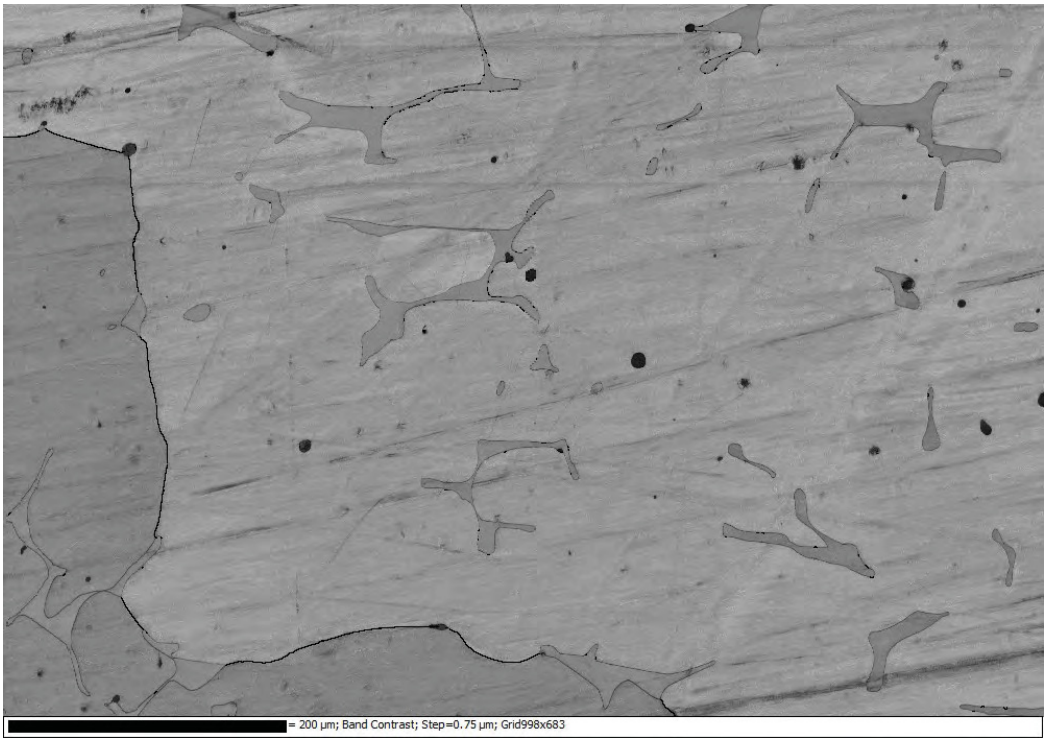

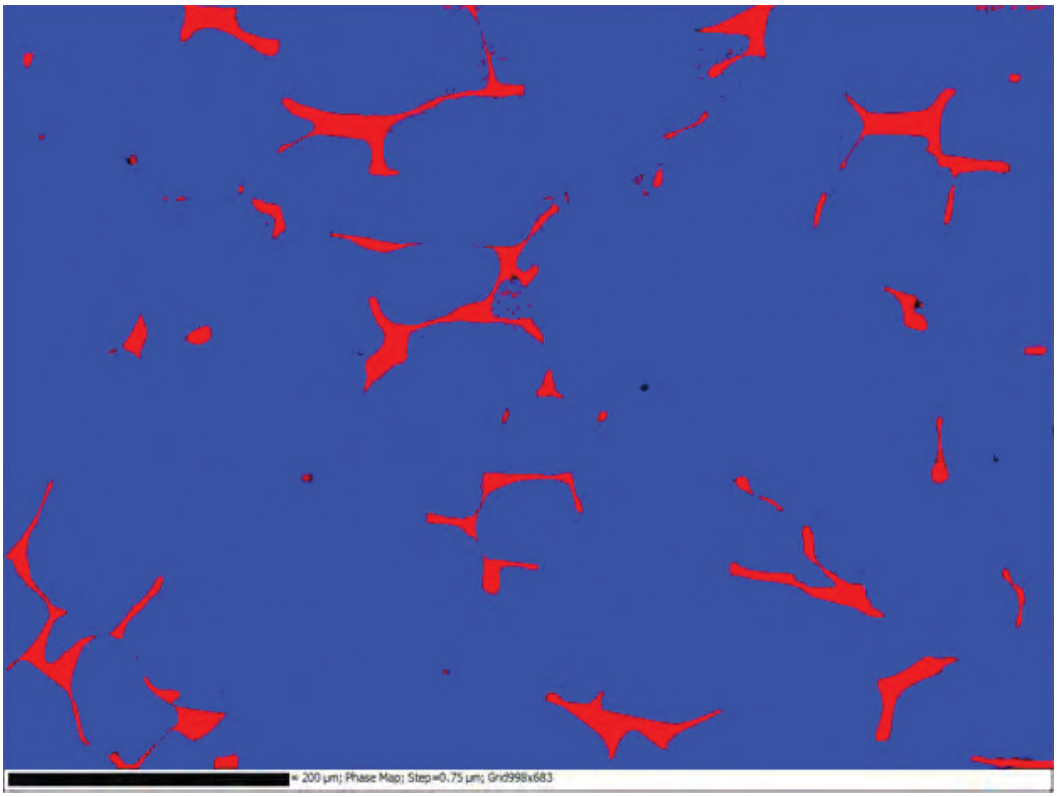

Pattern Quality (top), Phase Map (bottom)

Volume Fraction BCC Phase(red) = 6.0%

IPF-X

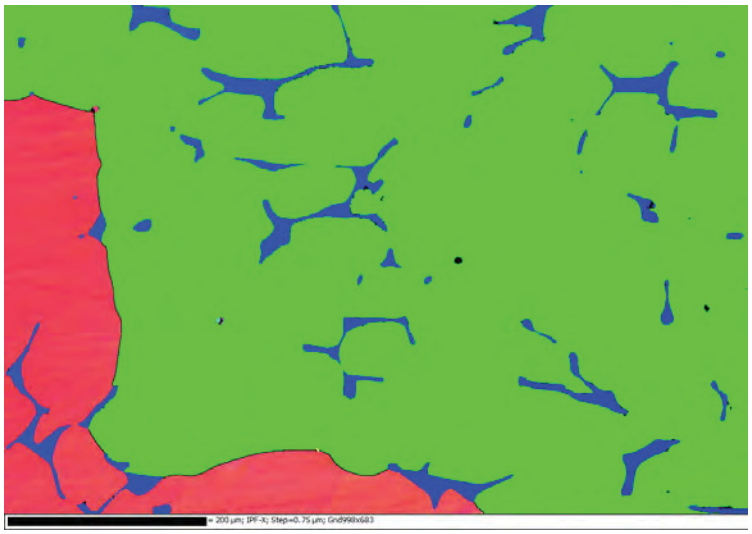

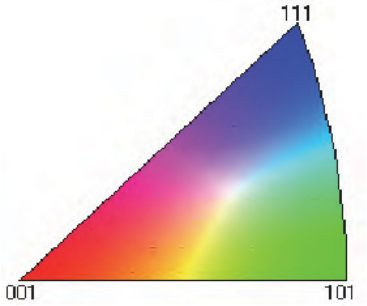

IPF-Y

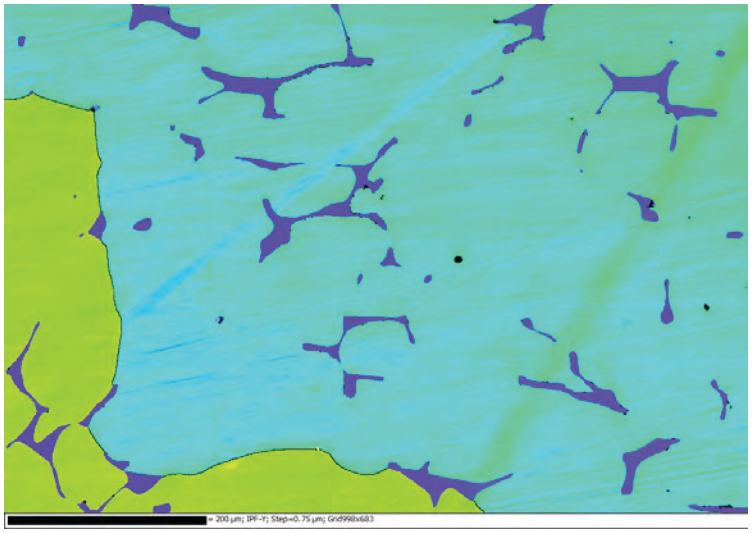

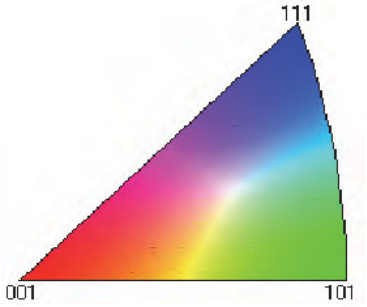

IPF-Z

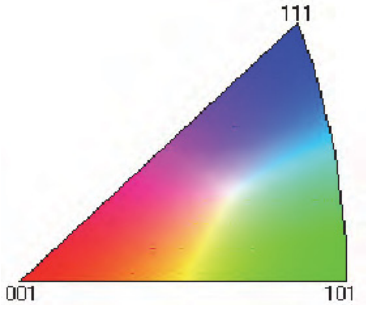

Specimen: CF8M (Block A, Fractured Specimen)

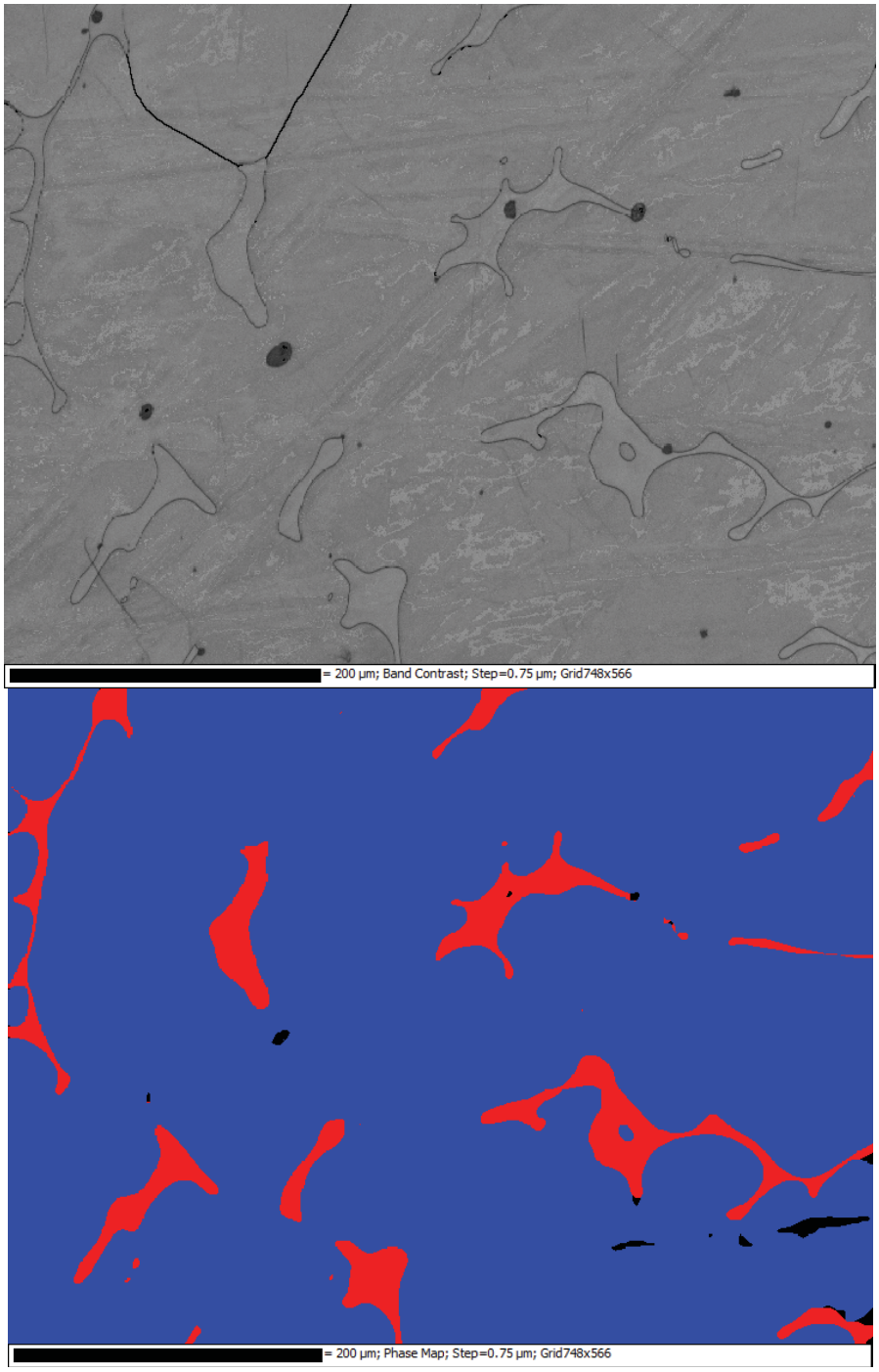

Pattern Quality (top), Phase Map (bottom)

Volume Fraction BCC Phase(red) = 7.2%

IPF-X

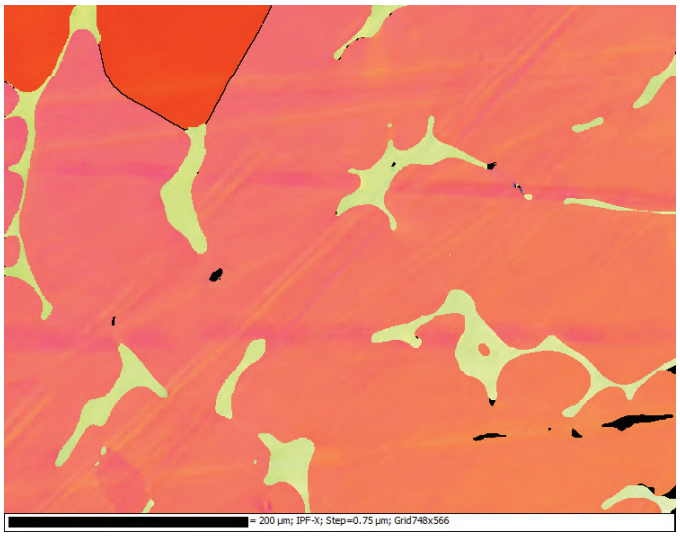

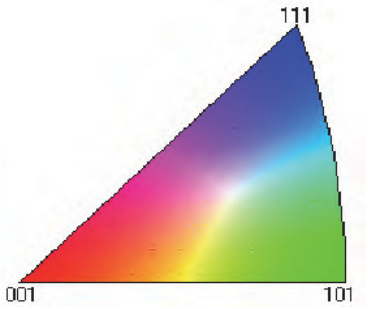

IPF-Y

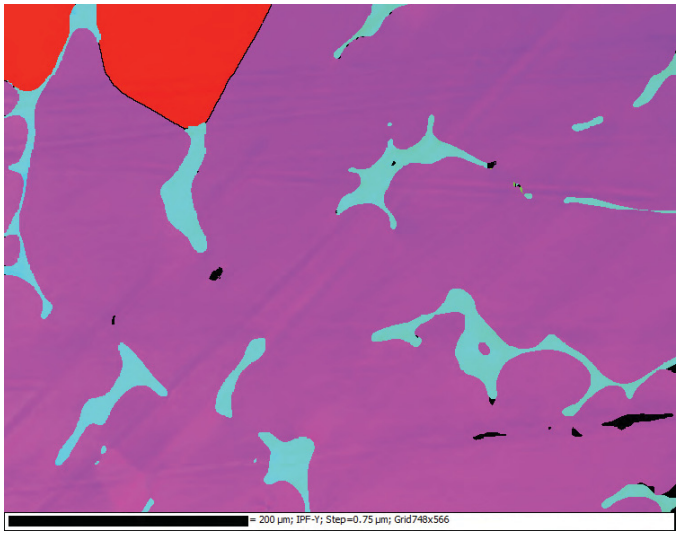

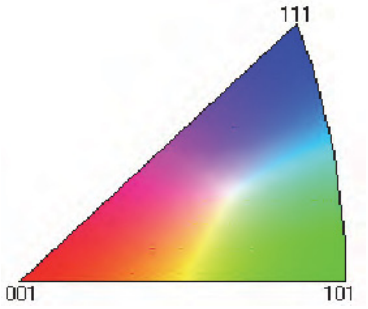

IPF-Z